Numerical Simulation of Liquid Crystalline Polymer Processing

Sun Jianye

A dissertation submitted to
Kochi University of Technology
in partial fulfillment of the requirements
for the degree of

Doctor of Philosophy

Special Course for International Students
Department of Engineering
Graduate School of Engineering
Kochi University of Technology
Kochi, Japan

March 2006

Abstract

The molecules of liquid crystal polymers (LCPs) are consisted of rigid and flexible monomers that link to each other. In shear flows, the rigid segments of the molecules usually tend to align in the direction of the flow. Once this orientation is formed, their direction and structure persist, even when LCP is cooled below the melting temperature. As a result of this unique structure, LCPs show many unusual properties, such as: high strength, good heat resistance, high impact resistance, and low stretch or elongation. At present, commercial uses of LCPs range from fibers for bulletproof vests, to packaging for electrical and optical components. Thermotropic LCPs are particularly attractive for injection molding, because of their low shrinkage and low viscosity in the nematic melt state.

At present, Leslie-Ericksen (L-E) theory and Doi's theory are the two popular constitutive theories for liquid crystals. The L-E theory, which is based on macroscopic continuum mechanics, is suitable for describing the rheological properties of low molecular weight nematics and polymer nematics at low shear rate. The Doi's theory, derived from microscopic molecular theory, is a kinetic model for rod-like polymers. Usually the Doi's model is too complicated to be used in the simulation of complex flows. Marrucci, Kuzuu and Doi have demonstrated that the Doi's theory could be reduced to the L-E theory in the limit of low shear rates. Many researchers have used the L-E theory in analyzing flow induced behaviour of LCPs.

The simulation of the LCPs flows during injection moulding in thin-walled moulds, which can be simplified by Hele-Shaw approximations, were investigated in this work. The Leslie- Ericksen equations of motion in the high viscosity limit were used to model the flows.

Space discretization is necessary for solving the governing equations. There are several ways to numerically approximate the partial differential equations, such as, finite difference method, finite element method, and boundary integral method. Among them, the finite difference method is the simplest one and it also has advantages with regard to computational time and storage. However, it is difficult for the finite difference method to treat flows in domains of complex shaped geometries. The numerical grid generation technique can remove the problem of boundary shape from

finite difference methods. This scheme has been used successfully in the finite difference solution of the equations for flows in irregularly shaped two-dimensional bodies by many researchers. However, the grid control is not a simple task for complicate geometries. To solve this problem, we developed the so-called " improved boundary-fitted mapping" technique, which is described in section 3.4.

This new scheme is much simpler than the original numerical grid generation technique. It frees the computational simulation from restriction to certain boundary shapes and allows general codes to be written in which the boundary shape is specified simply by input. It can help the finite difference method to overcome its difficulty on treating flows in complicated geometries and keep the simplicity and high efficiency of the finite difference method at the same time.

The simulation results are described in chapter 4. In section 4.2, we give an analysis of the steady director of liquid crystal in Hele-Shaw flows. This result may help to explain a widely recognized phenomenon in the molding process of nematic polymers, which is that the molecular chains in the skin regions are largely aligned along the injection direction while the chain orientation in the central core is more or less random.

List of content

Chapter 1: Introduction

1.1 Liquid crystals

1.1.1 Introduction

Liquid crystals are substances that exhibit a phase of matter that has properties between those of a conventional liquid and those of a solid crystal. As shown in figure 1-1, in liquid crystal state, the molecules possess at least some orientational order, but lack the full three-dimensional positional order of solid crystals. They were first observed by Friedrich Reinitzer, an Austrian botanist, in 1888 and named by Otto Lehman, a German physicist. Although for 100 years they had no practical uses, they were studied intently by several determined scientists, who learned many of their secrets. Since the 1960s, the knowledge they extracted has become very profitable. Now liquid crystals find wide uses, such as Liquid Crystal Displays, Liquid Crystal Thermometers, Optical Imaging, and many other applications.
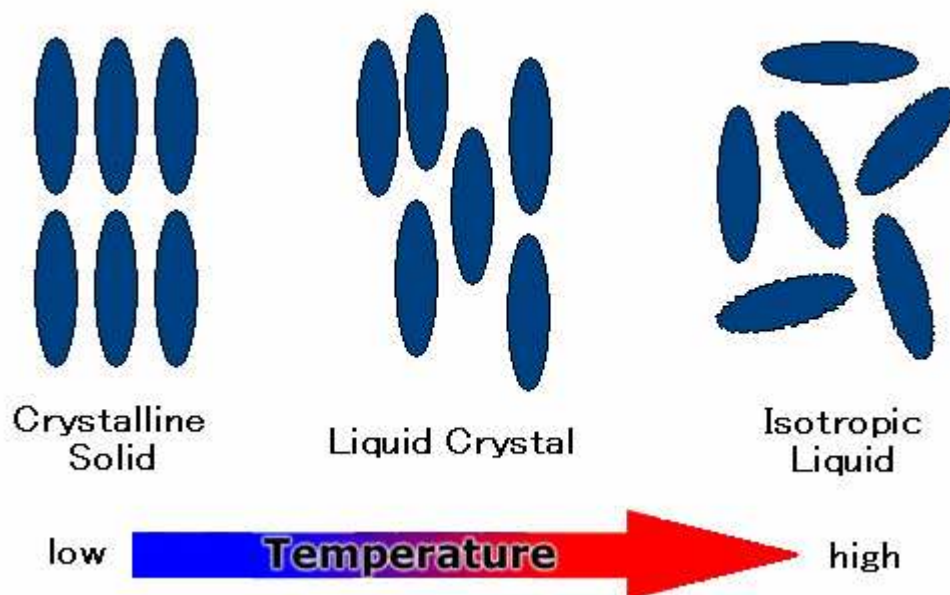

Fig 1-1 liquid crystal state

1.1.2 Liquid crystal phases [21]

Molecules that form liquid crystalline phase are often oblate or prolate in shape, because orientational order is possible for them. Crystalline solids made of such molecules can melt into isotropic liquids in multiple steps. At intermediate stages of the melting, there can be orientational order with no, or only partial positional order. That is, the molecules might tend to be aligned in a common direction, but the centers of mass of the molecules take on random positions. Such intermediate phases are liquid crystals. The various liquid crystal phases (called *mesophases*) can be characterized by the type of ordering that is present. One can distinguish positional order and orientational order, and moreover, order can be either short-range or long-range.
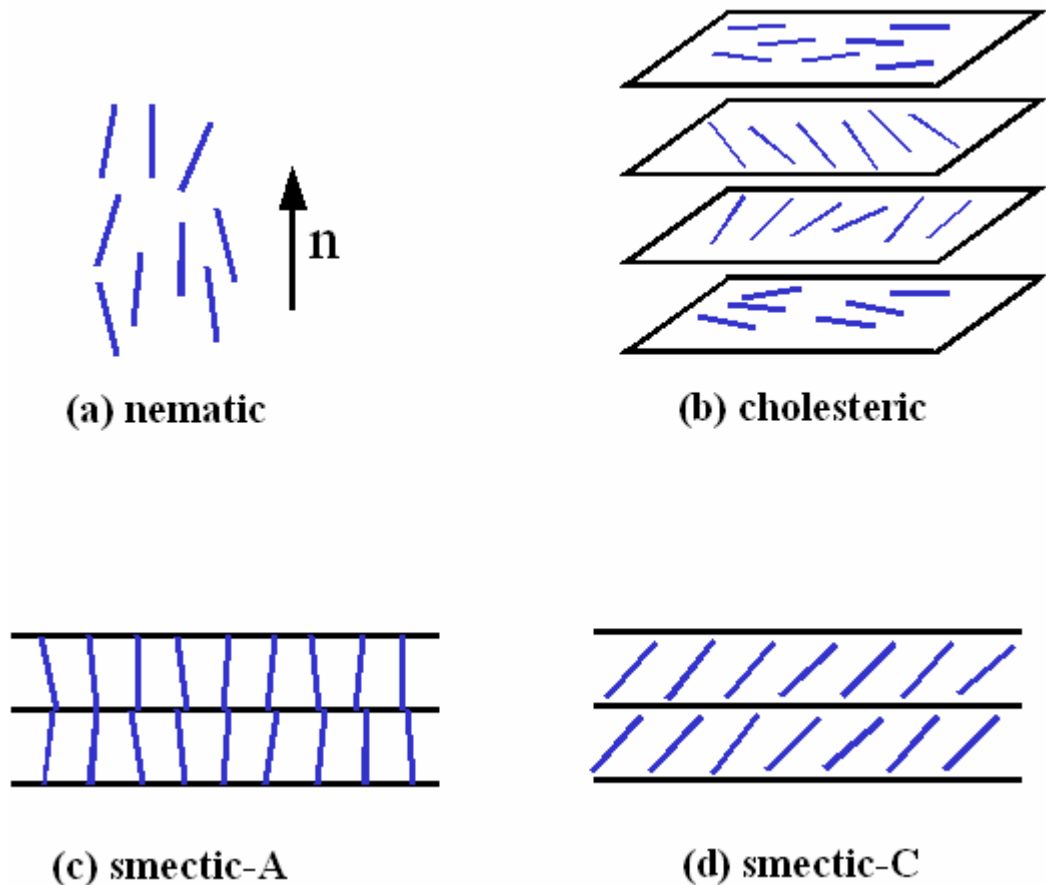

Fig 1-2 Schematic representations of liquid crystal phases

The ordering of liquid crystalline phases is extensive on the molecular scale. This order extends up to the entire domain size, which may be on the order of micrometer,

but usually does not extend to the macroscopic scale as often occurs in classical crystalline solids. However, some techniques (such as the use of boundaries or an applied electric field) can be used to enforce a single ordered domain in a macroscopic liquid crystal sample. The ordering in a liquid crystal might extend along only one dimension, with the material being essentially disordered in the other two directions.

Nematic phase

One of the most common liquid crystal phases is the nematic, which possess orientational, but no positional order. The direction of preferred orientation is designated by a unit vector called "director"**n**. As shown in figure 1-2(a), **n** gives the preferred average orientation in the neighbourhood of any point. Most nematics are uniaxial: they have one axis that is longer and preferred, with the other two being equivalent (can be approximated as cylinders). Some liquid crystals are biaxial nematics, meaning that in addition to orienting their long axis, they also orient along a secondary axis.

Cholesteric phases

Only chiral molecules (i.e.: those that lack inversion symmetry) can give rise to such a phase. As show in figure 1-2(b), this phase exhibits a twisting of the molecules along the director, with the molecular axis perpendicular to the director. The finite twist angle between adjacent molecules is due to their asymmetric packing, which results in longer-range chiral order.

The *chiral pitch* refers to the distance (along the director) over which the mesogens undergo a full 360° twist (but note that the structure repeats itself every half-pitch, since the positive and negative directions along the director are equivalent). The pitch may be varied by adjusting temperature or adding other molecules to the liquid crystal fluid. For many types of liquid crystals, the pitch is on the same order as the wavelength of visible light. This causes these systems to exhibit unique optical properties, such as selective reflection. These properties are exploited in a number of optical applications.

Smectic phase

The smectics are layered materials. They possess both orientational and one-dimensional, or layer-like, position order. The simplest smectic is the smectic-A phase, in which the molecules point perpendicular to the layer planes, whereas in the

smectic C phase, the molecules are tilted with respect to the layer planes, as shown in (c) and (d) of figure 1-2. In hexatic phases, the mesogens in a particular layer take on a roughly hexagonal close-packed ordering, with typically no registry between adjacent smectic layers. It is also possible to find examples of liquid crystals where the registry between layers is fairly strong; hence there is three-dimensional positional (and possibly even orientational) order. These phases are called crystal mesophases, and are in fact nearly as ordered as solid crystals (although they still exhibit fluid-like flow).

1.2 Liquid Crystal Polymers [13]

1.2.1 Introduction

Liquid crystal Polymers (LCPs) are a class of materials that combine the properties of polymers with those of liquid crystals. These "hybrids" show the same mesophases characteristic of ordinary liquid crystals, yet retain many of the useful and versatile properties of polymers. LCPs are commercially interesting because of their following properties:

- Low stretch or elongation
- Resistance to cutting
- Excellent thermal properties (esp. heat resistance)
- Difficult to wear away
- High strength
- Low weight
- High impact resistance

In addition, the process ability of LCPs is enhanced by the low viscosity they have in the nematic melt state, resulting from their chain stiffness and high molecular orientation. At present, the commercial uses of LCPs include fibers for bulletproof vests, packaging for electrical and optical components, and strong, lightweight aircraft parts, where the high cost of LCPs is not an overriding issue. In the future, there may be applications in the area of nonlinear optical components and, for side-group LCPs, in field-orientation devices (Donald and Windle 1992)

The molecules of LCPs are generally semirigid or contain rigid units, called mesogens. The distribution of orientations of the molecules, or at least of the mesogens, is anisotropic in the liquid crystalline state. The placement of the mesogens plays a large role in determining the type of LCPs that is formed. The main-chain LCPs or MC-LCPs are formed when the mesogens are themselves part of the main chain of a polymer. Conversely, in side chain LCPs or SC-LCPs the mesogens are attached to the backbone by flexible spacers.
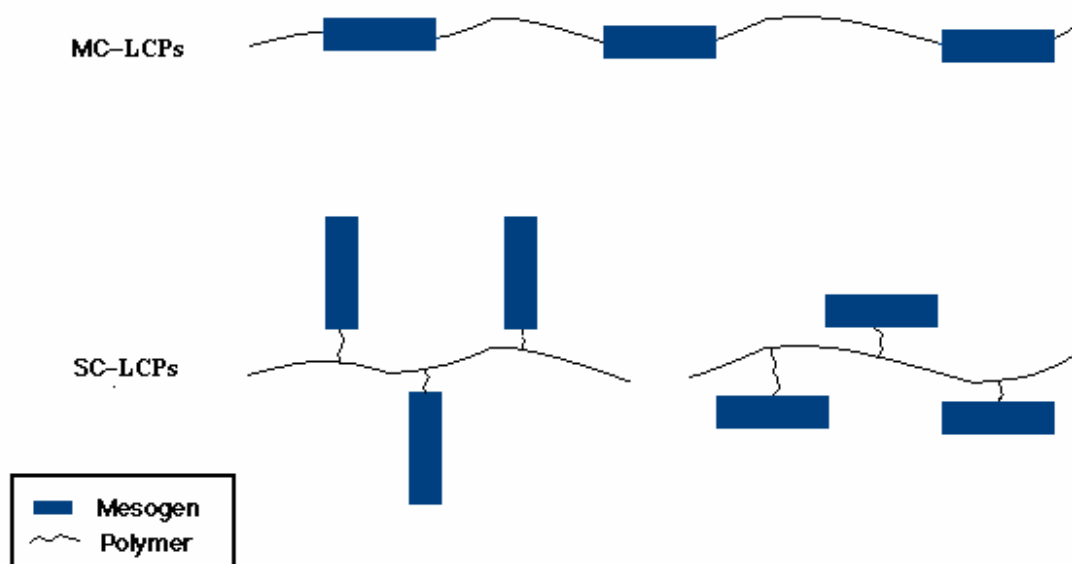

Fig 1-3 Schematic illustration of different kinds of polymers

Other factors influencing the mesomorphic behavior of polymers include the presence of long flexible spacers, a low molecular weight, and regular alternation of rigid and flexible units along the main chain.

1.2.2 Temperature Range Problems

In 1923, Vorlander synthesized long liquid-crystal-forming molecules by connecting benzene rings together at their para positions using esther linkages and found that the

melting point of these materials increases rapidly with increasing molecular length. This work culminated in the synthesis of poly(p-benzamide); its melting point, however, was so high that it charred before melting. The problem of achieving a lower melting temperature for such materials was finally overcome in 1976 by Jackson and coworkers at Eastman Kodak, by using random copolymers of aromatic polyesters.

The first method of lowering polymer melting temperatures involves the arrangement of the monomers in the chain. If the molecules are put together in random orientation (head-to-tail, head-to-head, etc.), interactions between successive chains are minimized. This allows for a lower melting temperature.

Another method to bring the temperature down to a useful range involves copolymerization. If a random copolymer can be created, the regularity of the chains is greatly reduced. This will help to minimize the interactions between the chains by breaking up the symmetry, which in turn will lower polymer melting temperature.

Finally, defects can be introduced into the chain structure which lower the polymer melting temperature. This method creates 120 degree "kinks" in the chain which disrupt the ability for neighboring polymers to line up. Unfortunately, this also decreases the effective persistence length. At same time, too many kinks can destroy any liquid crystal behavior.

1.3 Applications of Liquid Crystal Polymers [13]

At present, commercial applications of LCPs range from the production of high-strength materials to optical devices. The following is an introduction to some of these applications.

1.3.1 High-Strength Fibers

Because of their chain stiffness and high molecular orientation, LCPs show unusual bulk properties. Solidified LCP fibers can have tensile moduli in the tens or hundreds of gigapascals and can have fracture strengths of order 1-4 GPa [11].. Kevlar, which is

used to make such things as helmets and bullet-proof vests, is just one example of the use of polymer liquid crystals in applications calling for strong, light weight materials.

Ordinary polymers have never been able to demonstrate the stiffness necessary to compete against traditional materials like steel. It has been observed that polymers with long straight chains are significantly stronger than their tangled counterparts. Main chain liquid crystal polymers are well-suited to ordering processes. For example, the polymer can be oriented in the desired liquid crystal phase and then quenched to create a highly ordered, strong solid. As these technologies continue to develop, an increasing variety of new materials with strong and light-weight properties will become available.

1.3.2 Optical Applications

At present, most liquid crystal displayers are made of traditional liquid crystals. However, the use of LCPs in the display industry is an exciting area of research, because the manipulation of polymers is often much easier than traditional liquid crystals. At this time, the main shortage of liquid crystal polymer displayer is their slow "response time" to electrical fields. Researchers are working to overcome this problem.

In addition, Side chain polymer liquid crystals exhibit good properties for applications in optically nonlinear devices including optical waveguides and electro-optic modulators in poled polymeric slab waveguides. More devices are expected to be fabricated from LCPs in the future: optically-addressed spatial light modulators, tunable notch filters, optical amplifiers, and laser beam deflectors. The properties of ferroelectric chiral smectic C phases make this material useful for films with applications in nonlinear optics.

Chapter 2: Constitutive model

The Leslie-Ericksen (L-E) theory (Leslie 1966; de Gennes and Prost 1993) offers a general relationship that satisfies the symmetry properties of uniaxial nematics fluids with a single director, for which the stress is linear in the local velocity gradient. It can be applied to small-molecule nematics and polymeric nematics at low shear rate.

2.1 Ericksen Transversely Isotropic Fluid [11]

The stress tensor for a flowing nematic which neglects elasticity is given as (Ericksen 1960, 1961):

$$\boldsymbol{\tau} = \beta_0 \mathbf{A} + \beta_1 \mathbf{n} \cdot \mathbf{A} \cdot \mathbf{nnn} + \beta_2 (\mathbf{nn} \cdot \mathbf{A} + \mathbf{A} \cdot \mathbf{nn}) \tag{2-1}$$

and the director evolution become:

$$\frac{D\mathbf{n}}{Dt} = \mathbf{W} \cdot \mathbf{n} + \lambda (\mathbf{A} \cdot \mathbf{n} - \mathbf{n} \cdot \mathbf{A} \cdot \mathbf{nn}) \tag{2-2}$$

where

$$\frac{D\mathbf{n}}{Dt} = \frac{\partial \mathbf{n}}{\partial t} + \mathbf{v} \cdot \nabla \mathbf{n} \tag{2-3}$$

Here $\mathbf{n}$ is the director, $\mathbf{A}$ is the rate of strain tensor, and $\mathbf{W}$ is the vorticity tensor,

$$\mathbf{A} = \frac{\nabla \mathbf{v} + (\nabla \mathbf{v})^T}{2} \tag{2-4}$$

$$\mathbf{W} = \frac{\nabla \mathbf{v} - (\nabla \mathbf{v})^T}{2} \tag{2-5}$$

and β_0, β_1, and β_2 are constant viscosities.

The coefficient λ is called the reactive parameter, or tumbling parameter, it controls the rotation of the director in a flow field. It is a function of Leslie coefficients.

$$\lambda = \frac{\alpha_2 + \alpha_3}{\alpha_2 - \alpha_3} \tag{2-6}$$

Consider a simple shearing flow, and define x to be the flow direction, y to be the velocity gradient direction, and z to be the vorticity direction. In a flow like this, $v_y = v_z = 0$, $\partial v_x / \partial z = \partial v_x / \partial x = 0$. Therefore

$$\mathbf{W} = \frac{\nabla \mathbf{v} - (\nabla \mathbf{v})^T}{2} = \frac{1}{2}\left(\begin{bmatrix} 0 & \dfrac{\partial v_x}{\partial y} & 0 \\ 0 & 0 & 0 \\ 0 & 0 & 0 \end{bmatrix} - \begin{bmatrix} 0 & 0 & 0 \\ \dfrac{\partial v_x}{\partial y} & 0 & 0 \\ 0 & 0 & 0 \end{bmatrix}\right) = \frac{1}{2}\begin{bmatrix} 0 & \dfrac{\partial v_x}{\partial y} & 0 \\ -\dfrac{\partial v_x}{\partial y} & 0 & 0 \\ 0 & 0 & 0 \end{bmatrix} \tag{2-7}$$

$$\mathbf{A} = \frac{\nabla \mathbf{v} + (\nabla \mathbf{v})^T}{2} = \frac{1}{2}\left(\begin{bmatrix} 0 & \dfrac{\partial v_x}{\partial y} & 0 \\ 0 & 0 & 0 \\ 0 & 0 & 0 \end{bmatrix} + \begin{bmatrix} 0 & 0 & 0 \\ \dfrac{\partial v_x}{\partial y} & 0 & 0 \\ 0 & 0 & 0 \end{bmatrix}\right) = \frac{1}{2}\begin{bmatrix} 0 & \dfrac{\partial v_x}{\partial y} & 0 \\ \dfrac{\partial v_x}{\partial y} & 0 & 0 \\ 0 & 0 & 0 \end{bmatrix} \tag{2-8}$$

$$\mathbf{nn} : \mathbf{A} = \sum_{i=1,3}\sum_{j=1,3} n_i n_j A_{i,j} = n_x n_y \frac{\partial v_x}{\partial y} \tag{2-9}$$

Then equation (2-2) turn to

$$\frac{D\mathbf{n}}{Dt} = \begin{bmatrix} \dot{\gamma}(\dfrac{n_y}{2}(\lambda + 1) - \lambda n_x{}^2 n_y) \\ \dot{\gamma}(\dfrac{n_x}{2}(\lambda - 1) - \lambda n_y{}^2 n_x) \\ -\lambda n_x n_y n_z \dot{\gamma} \end{bmatrix} \tag{2-10}$$

The director $\mathbf{n}$ can be represented in terms of a polar angle θ and an aximuthal angle φ as $\mathbf{n} = (n_x, n_y, n_z) = (\cos\theta\cos\varphi, \sin\theta\cos\varphi, \sin\varphi)$.

set $D\mathbf{n}/Dt = \mathbf{0}$, we can get the steady-state solution for $|\lambda| > 1$:

$$n_z = \sin\varphi = 0 \tag{2-11}$$

$$\tan\theta = \pm(\frac{\lambda - 1}{\lambda + 1})^{1/2} \tag{2-12}$$

There are four such steady-state solution in the (n_x, n_y) plane, as depicted in the figure 2-1. Since nematics are nonpolar, two of the four solutions shown in figure 2-1 are redundant; of the remaining two solution, one is unstable and the other stable. For $\lambda > 1$ and a shear rate that is positive, the stable solution is the one with a positive sign in equation (2-12).

If $|\lambda| < 1$, equation (2-10) has no steady-state solutions in the shearing plane. And the director rotates endlessly in the deformation plane. When $|\lambda| < 1$ the nematics is called a tumbling nematics, while when $|\lambda| > 1$, the nematics is flow-aligning.
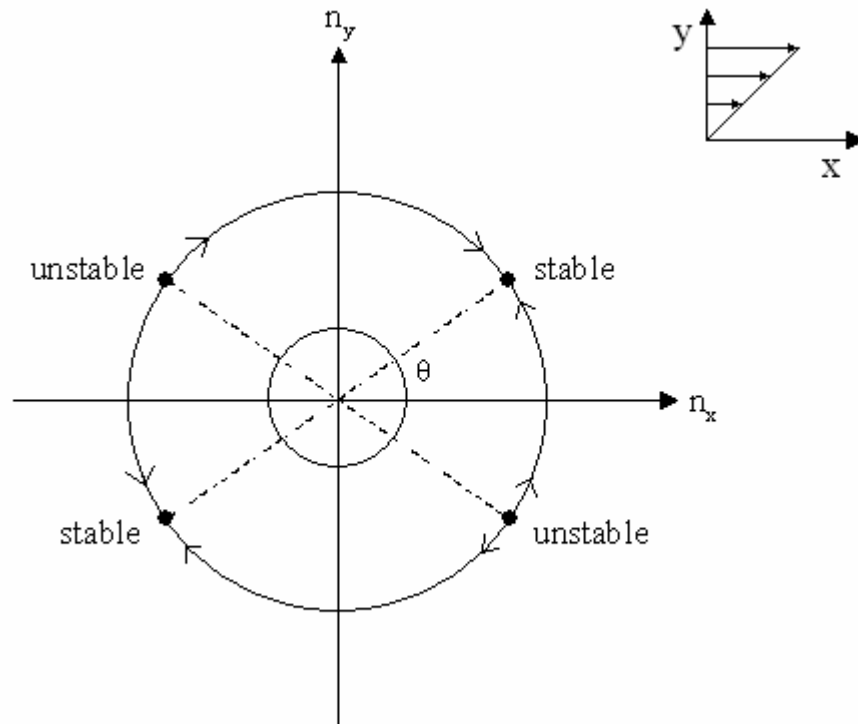

Fig 2-1 Ericksen diagram showing directions of rotation and directors of steady state

2.2 Frank-Oseen Theory

The liquid crystal molecules in the nematic phase tend to follow a preferred direction of alignment. However, spatial variations in the director field exist in real flows. It will disrupt somewhat the molecular packing and thus incur a free-energy penalty F, the minimization of which influences the equilibrium or static dependence of the director **n** on position. If the change of the director orientation is small over the

length of a molecule, then the excess free energy density F produced by that gradient can be obtained from the low-order Frank continuum theory. According to the low-order Frank continuum theory, the excess free energy density F produced by that gradient can be written as:

$$2F = K_1(\nabla \cdot \mathbf{n})^2 + K_2(\mathbf{n} \cdot \nabla \times \mathbf{n})^2 + K_3 \|\mathbf{n} \times \nabla \times \mathbf{n}\|^2 \tag{2-13}$$

Here $\nabla \cdot \mathbf{n}$ and $\nabla \times \mathbf{n}$ are the divergence and curl of $\mathbf{n}$, K_i, i=1,2,3, correspond to the splay, twist and bend elasticity constants. The three contributions to F are associated with the three independent modes of distortion: splay, twist, and bend. This equation is valid when the change of the director orientation is small over the length of a molecule. The Frank constants K_1, K_2, and K_3 are of the order u/α, where α is a molecular length scale (actually the molecule's volume divided by its length squared) and u is a nematic interaction energy parameter.

2.3 Leslie-Ericksen Theory

In Leslie-Ericksen theory, both the viscous stresses and Frank elastic stresses are considered. It consists of two major equations: the stress tensor equation (2-14) and director rotate equation (2-17).

$$\boldsymbol{\tau} = \alpha_1 \mathbf{nnnn} : \mathbf{A} + \alpha_2 \mathbf{nN} + \alpha_3 \mathbf{Nn} + \alpha_4 \mathbf{A} + \alpha_5 \mathbf{nn} \cdot \mathbf{A} + \alpha_6 \mathbf{A} \cdot \mathbf{nn} \tag{2-14}$$

Here $\alpha_1, \alpha_2, ..., \alpha_6$ are the six constant viscosities (the Leslie coefficients).

$$\alpha_6 = \alpha_2 + \alpha_3 + \alpha_5 \tag{2-15}$$

In equation (2-14), $\mathbf{N}$ is defined as

$$\mathbf{N} \equiv \frac{D\mathbf{n}}{Dt} - \mathbf{n} \cdot \mathbf{W} \tag{2-16}$$

$\mathbf{N}$ is the rotation rate of $\mathbf{n}$ relative to that of the background fluid.

$$\mathbf{n} \times \left\{ \frac{\partial F}{\partial \mathbf{n}} - \nabla \cdot (\frac{\partial F}{\partial \nabla \mathbf{n}}) - (\alpha_2 - \alpha_3)\mathbf{N} + (\alpha_2 + \alpha_3)\mathbf{A} \cdot \mathbf{n} \right\} = \mathbf{0} \tag{2-17}$$

Chapter 3: Numerical techniques [15]

3.1　Introduction

Space discretization is necessary for solving the governing equations. It involves the approximation of velocities, pressures, and temperatures at prescribed values of x and y on a spatial grid. For non-Newtonian flow problems, the required approximation is usually generated by using finite difference and finite element methods, both of which are well established.

The finite difference approach is the easier of the two to implement and its background mathematical analysis is also relatively simple. Further, finite difference technique has advantages with regard to computational time and storage.

The development of a finite element code requires a non-negligible amount of programming, however, the initial difficulties associated with this approach can be compensated to some extent by the ease by which a finite element code, once written, can be changed to accommodate new flow situations and geometries. Furthermore, finite element method implements natural boundary conditions and complex geometries can be handled with relative ease.

In general, the finite difference method is simple and high efficient. However, it is difficult for the finite difference method to treat flows in domains of complicated shaped geometries. In this study, the finite difference method was selected for space discretization, and a new "improved boundary-fitted mapping" technique (described in section 3.4) was developed to treat flows in complicated geometries.

3.2　Finite difference Method

3.2.1 Introduction

The governing equations of liquid crystal polymer flows are a set of partial difference equations, which are usually solved numerically. Discretization process, which converts the partial difference equations into a set of algebraic equations, is the

basic technology for numerically solution of partial difference equations. These algebra equations can provide the field variable values at discrete points within the domain. At present, finite element, finite difference, and boundary element techniques are the three primary approaches for discretization process. Among them, the finite difference method is the most common and conceptually straightforward method of discretization for field variables defined on grid points. Finite difference methods originated in the 1930's for hand calculation; their use expanded rapidly with the development of digital computers. Despite their limitations, traditional finite difference techniques still represent the most developed and best understood numerical procedure for solving partial differential equations.

A finite difference solution to a field problem involves three steps. First, a grid is constructed over the flow domain. Second, the governing partial difference equations are converted into a set of algebraic equations, which are algebraic expressions for the nodal values of the problem variables. Finally, the algebraic equations obtained in step two are solved numerically.
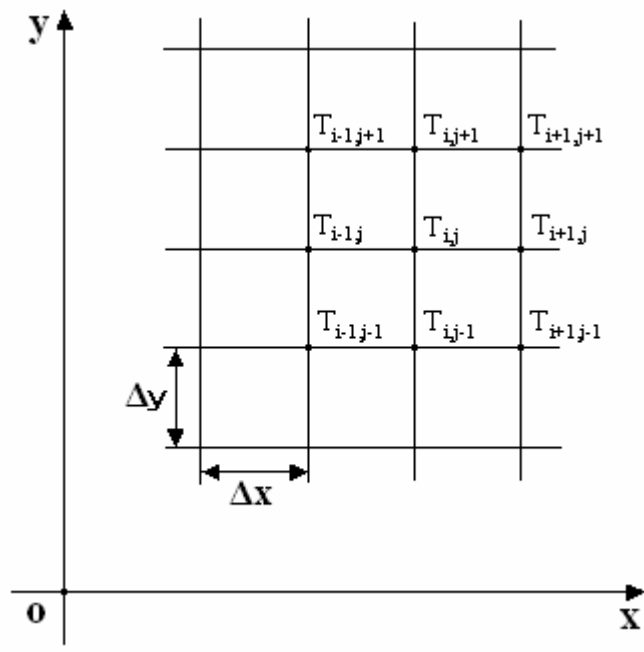

Fig 3-1 Construction of a mesh over the problem domain and identification
of nodal points using indices

3.2.2 Basic formulations

Taylor series expansion is the most basic approach to formulate discrete finite difference equations. It can predict truncation errors to compare the accuracy of different discretization formulas. Consider a quantity T which is a function of independent variables, x and y. T is defined at equally spaced, discrete grid points (x_i, y_j) on the Cartesian mesh shown in figure 3-1. We look for an approximation to the derivative $\partial T/\partial x$ at a grid point. The indices i,j identify the nodal locations in x and y directions respectively. Assume $T_{i,j}$ stands for the value of T at a grid point (x_0, y_0). If the function T is continuous over the domain, then the value of $T_{i+1,j}$ can be expressed in term of $T_{i,j}$ by a Taylor series expansion.

$$T_{i+1,j} = T_{i,j} + \frac{\partial T}{\partial x}\Big|_{i,j}(\Delta x) + \frac{\partial^2 T}{\partial x^2}\Big|_{i,j}\frac{(\Delta x)^2}{2!} + \frac{\partial^3 T}{\partial x^3}\Big|_{i,j}\frac{(\Delta x)^3}{3!} + \cdots \tag{3-1}$$

From the above equation, we can get the first order derivative of T at the location (x_0, y_0) as:

$$\frac{\partial T}{\partial x}\Big|_{i,j} = \frac{T_{i+1,j} - T_{i,j}}{\Delta x} - \frac{1}{2}\frac{\partial^2 T}{\partial x^2}\Big|_{i,j}\Delta x + \cdots \tag{3-2a}$$

or

$$\frac{\partial T}{\partial x}\Big|_{i,j} = \frac{T_{i+1,j} - T_{i,j}}{\Delta x} + O(\Delta x) \tag{3-2b}$$

where $O(\Delta x)$ indicates the order of the additional terms in the series. It means this equation has a truncation error of order Δx. The nature of the Taylor series expansion lets higher order terms be truncated because magnitudes of the higher order terms are smaller. Dropping these additional terms gives an expression for the first order derivative of T at the point (x_0, y_0):

$$\frac{\partial T}{\partial x}\Big|_{i,j} = \frac{T_{i+1,j} - T_{i,j}}{\Delta x} \tag{3-3}$$

Equation (3-3) is called a forward difference expression for the first order derivative because equation (3-1) expanded the function T in the positive x-direction. The elimination of higher order terms in the Taylor series introduces a truncation error. Equation (3-3) is no longer exact, but contains an error of order Δx. Similarly, we can

get the backward difference expression and central difference expression shown in equation (3-4) and equation (3-5).

$$\frac{\partial T}{\partial x}\bigg|_{i,j} = \frac{T_{i,j} - T_{i-1,j}}{\Delta x} + O(\Delta x) \tag{3-4}$$

$$\frac{\partial T}{\partial x}\bigg|_{i,j} = \frac{T_{i+1,j} - T_{i-1,j}}{2\Delta x} + O(\Delta x^2) \tag{3-5}$$

It can be seen that the backward and forward difference expressions have an error of order Δx. However, the central difference expression has a truncation error of order Δx^2.

The Taylor series expansions at two nodes are necessary to approximate the second order derivative $\partial^2 T/\partial x^2$ at the grid point (x_0, y_0).

$$T_{i+1,j} = T_{i,j} + \frac{\partial T}{\partial x}\bigg|_{i,j}(\Delta x) + \frac{\partial^2 T}{\partial x^2}\bigg|_{i,j}\frac{(\Delta x)^2}{2!} + \frac{\partial^3 T}{\partial x^3}\bigg|_{i,j}\frac{(\Delta x)^3}{3!} + \cdots \tag{3-6a}$$

$$T_{i-1,j} = T_{i,j} - \frac{\partial T}{\partial x}\bigg|_{i,j}(\Delta x) + \frac{\partial^2 T}{\partial x^2}\bigg|_{i,j}\frac{(\Delta x)^2}{2!} - \frac{\partial^3 T}{\partial x^3}\bigg|_{i,j}\frac{(\Delta x)^3}{3!} + \cdots \tag{3-6b}$$

Add two above equations together,

$$T_{i+1,j} + T_{i-1,j} = 2T_{i,j} + \frac{\partial^2 T}{\partial x^2}\bigg|_{i,j}(\Delta x)^2 + O(\Delta x^4) \tag{3-7}$$

Then the approximation of $\partial^2 T/\partial x^2$ of second order accuracy is:

$$\frac{\partial^2 T}{\partial x^2} = \frac{T_{i+1,j} + T_{i-1,j} - 2T_{i,j}}{\Delta x^2} + O(\Delta x^2) \tag{3-8}$$

Similarly, we can get approximations of other second order derivative of function T at (x_0, y_0).

$$\frac{\partial^2 T}{\partial y^2} = \frac{T_{i,j+1} + T_{i,j-1} - 2T_{i,j}}{\Delta y^2} + O(\Delta x^2) \tag{3-9}$$

$$\frac{\partial^2 T}{\partial x \partial y} = \frac{T_{i+1,j+1} - T_{i-1,j+1} - T_{i+1,j-1} + T_{i-1,j-1}}{4\Delta x \cdot \Delta y} + O(\Delta x^2) \tag{3-10}$$

3.3 Boundary-fitted mapping technique

Numerical grid generation has been used by many researchers in the numerical solution of partial differential equations on arbitrarily shaped region. It can remove the problem of boundary shape from finite difference methods and serve for the construction of finite element meshes.

Numerical grids can be generated by mapping the irregular shaped geometry to a more regular shape in a computational domain. An orthogonal, rectangular mesh can be created in the transformed, simpler domain and then mapped back to provide a curvilinear mesh in the original irregular shape. The governing equations are similarly transformed and solved in the computational domain. The solutions at every node then are mapped back onto the original physical domain.

Here is an example of numerical grid generation. As shown in figure 3-2, first, divide the boundary of the physical domain into four segments: ab, bc, cd, and da. Then map these four segments onto the four sides of the rectangular a'b'c'd' in the computational domain: ab to a'b', bc to b'c', cd to c'd', and da to d'a'. Build an orthogonal rectangular mesh inside the rectangular a'b'c'd' and map it back into the original physical domain. We can get the curvilinear mesh in the physical domain, whose coordinate line (surface in 3D) is coincident with each segment of the boundary of the irregular shaped geometry.
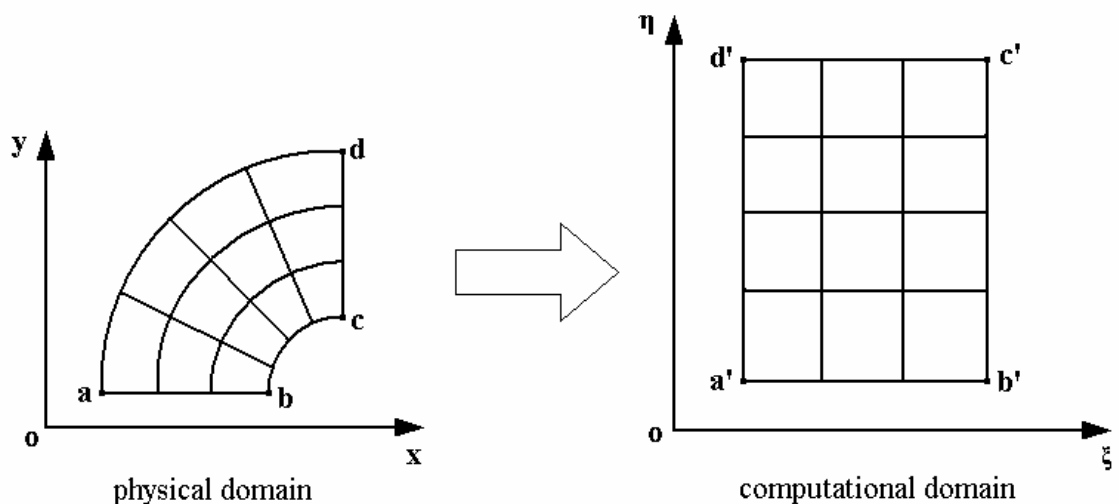

Fig 3-2 Mapping of the irregular physical domain to a regular computational domain

The generation of field values of a function from grid values can be done in various ways, e.g., by interpolation, etc.

The solutions of a system of partial differential equations are usually taken as the mapping function. If the coordinate points are specified on the entire closed boundary of the physical region, the equations must be elliptic, while if the specification is on only a portion of the boundary the equations could be parabolic or hyperbolic. In this study, we treat the general case of a completely specified boundary, which requires an elliptic partial differential system.

The elliptic partial differential system has two advantages. One is that the extremum principles exhibited by some elliptic systems can serve to guarantee a one-to-one mapping between the physical and transformed regions. Another important property in regard to coordinate system generation is the inherent smoothness that prevails in the solutions of elliptic systems.

A. Laplace system

The most simple elliptic partial differential system, and one that does exhibit an extremum principle and considerable smoothness is the Laplace system:

$$\frac{\partial^2 \xi}{\partial x^2} + \frac{\partial^2 \xi}{\partial y^2} = 0 \tag{3-11a}$$

$$\frac{\partial^2 \eta}{\partial x^2} + \frac{\partial^2 \eta}{\partial y^2} = 0 \tag{3-11b}$$

This generation system guarantees a one-to-one mapping for boundary-conforming curvilinear coordinate systems on general closed boundaries.

Because of the strong smoothing effect of the Laplacian, the coordinate lines will tend to be equally spaced in the absence of boundary curvature and in the regions away from the boundaries. However, they will become more closely spaced over convex boundaries, and less so over concave boundaries, as illustrated below.

At convex boundary, we have $\eta_{xx} > 0$, it follows that $\eta_{yy} < 0$. $\eta_{yy} < 0$ means the spacing between the η-lines will increase with y near the convex boundary. Consider the fact that the coordinate lines will tend to be equally spaced in the regions away from the

boundaries, we can get the conclusion that the η-lines thus will tend to be more closely spaced over a convex boundary segment, as shown in the left figure of figure 3-3. For concave segments, illustrated in the right figure of figure 3-3, we have $\eta_{xx} < 0$, so that η_{yy} must be positive, and hence the spacing of the η-lines must decrease outward from this concave boundary. Therefore, the irregular shaped geometry may cause unevenly distribution of the grids in physical domain.
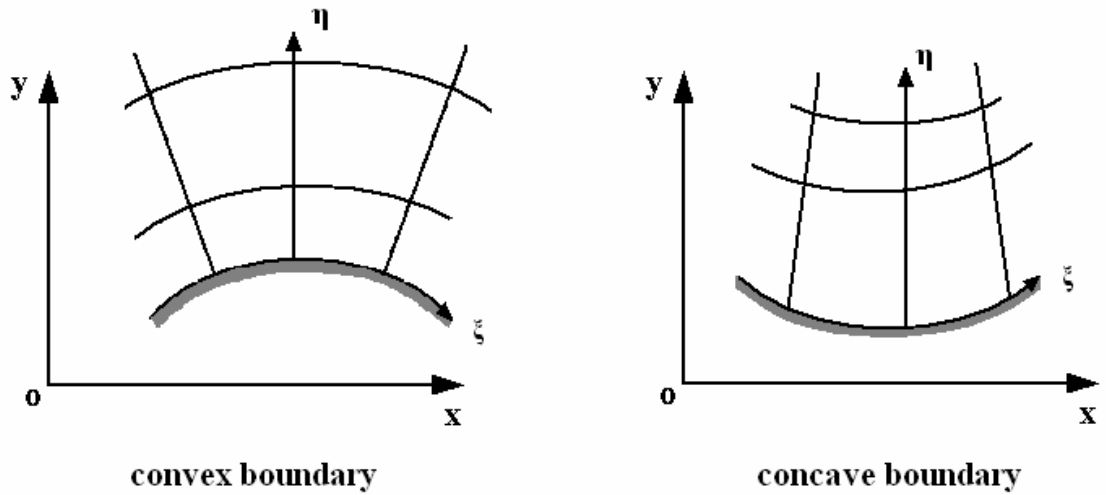

convex boundary   concave boundary

Fig 3-3 Coordinate lines near convex boundary and concave boundary

B. Poisson system

The control of grid distribution inside the flow domain can be solved by Poisson equations:

$$\frac{\partial^2 \xi}{\partial x^2} + \frac{\partial^2 \xi}{\partial y^2} = P \tag{3-12a}$$

$$\frac{\partial^2 \eta}{\partial x^2} + \frac{\partial^2 \eta}{\partial y^2} = Q \tag{3-12b}$$

in which P and Q are grid distribution control functions. The extremum principles may be weakened or lost completely with such a system, but the existence of an extremum principle is a sufficient, but not a necessary, condition for a one-to-one mapping, so that some latitude can be taken in the form of the control functions.

If Poisson equations are used in example shown in figure 3-3, we can use positive Q at convex boundary and minus Q at concave boundary to overcome to some extent the unevenly distribution caused by irregular shape of the flow domain.
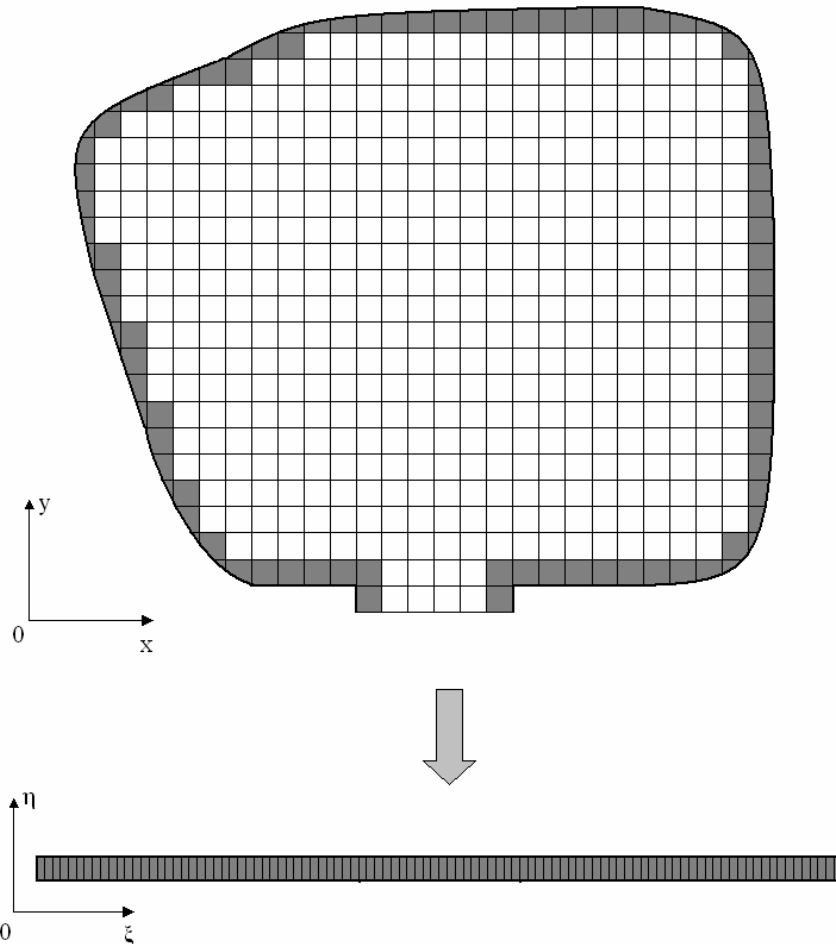

Fig 3-4   The numerical mapping of the boundary of irregular domain (from the physical x,y coordinates) to a more regular computational domain (in the ξ,η coordinates).

3.4 Improved Boundary-fitted mapping technique

Usually Poisson type elliptic expressions are used to relate the physical (x,y) coordinates to the computational (ξ,η) coordinates due to their inherent "smoothness" and ability to handle boundary discontinuities. These relations are shown in equation (3-12a) and (3-12b). Here P and Q are grid control functions that can be used to specify

mesh concentration in desired areas.

This scheme has been used successfully in the finite difference solution of the flows in irregularly shaped two-dimensional bodies by many researchers. However, it has two shortcomings. The first one is that it is difficult to determine P and Q. Many researchers just set P and Q as zero. It works well for some situations, but grid control is still necessary for complicated geometries. Another shortcoming is that it influences the simulation accuracy. The mapping cause extra errors.

To solve these two problems, we developed the improved boundary-fitted mapping technique. As shown in figure 3-4, only the boundary region of the flow domain (the shaded region) takes part in the mapping. There are no grids inside the mapping region, the mesh concentration control is not necessary and P and Q can be set equal to zero for arbitrarily shaped flow domains. Therefore, this new technique can solve the grid control problem of the original boundary-fitted mapping method.

At the grid nodes in the boundary region, the governing equations are transformed and solved in the computational domain, and the solutions at every node in the boundary region are mapped back into the physical domain. At the grid nodes in the flow domain other than the boundary region, the governing equations are solved in the physical domain directly. Because only a very small part of flow domain takes part in the mapping process, the extra errors caused by the mapping are much smaller than the ordinary boundary-fitted mapping technique. Therefore, the new mapping technique can also solve the accuracy problem of the ordinary boundary-fitted mapping technique to a great extent.

This new mapping technique is the most important result in this study. It is simple and easy to implement, its computational cost is low, and its accuracy is high. It frees the computational simulation from restriction to certain boundary shapes and allows general codes to be written, in which the boundary shape is specified simply by input. It can help the finite difference method to overcome its difficulty on treating flows in complicated geometries and keep the simplicity and high efficiency of the finite difference method at the same time.

Chapter 4: Simulation of Hele-Shaw flows

4.1 Hele-Shaw approximations

Most injection molded plastic parts are geometrical configurations of complicated shape and the rheological response of polymer melts is generally non-Newtonian and non-isothermal. Because of these inherent factors, it is extremely difficult to analyze the filling process without simplifications. The Generalized Hele-Shaw(GHS) flow model introduced by Hieber and Shen provides simplified governing equations for non-isothermal, non-Newtonian and inelastic flow in thin cavities.

Consider the flow of polymer melt through a mold cavity with a high aspect ratio cross-section, which varies in dimension along its length. The melt flows in x-y plane, the z-direction is perpendicular to the flow field, and h(x,y) is the local separation between the mold surfaces. Since the separation between the surfaces is typically much smaller than the other dimensions, one would expect that the flow at a given point be mostly influenced by the local geometry. Therefore, the lubrication approximation can be applied: the velocity component in z-direction can be neglected and the pressure is a function of x and y only. Moreover, due to the extremely high viscosity of the polymer melt, the flow regions are considered to be fully developed Hele-Shaw flows in which inertia and gravitational forces are much smaller than viscous forces. The flow kinematics are shear-dominated and the shear viscosity is taken to both temperature and shear rate dependent. Because of these approximations, a GHS model cannot predict the exact flow field near the advancing flow front or at the edges of the mold. However, these regions extend only a thin layer of order h in the horizontal plane.

4.2 Analysis of the steady director of liquid crystal in Hele-Shaw flow

In this section, the center of a fully developed symmetric expansion Hele-Shaw flow, shown in figure 4-1, was considered. In this flow, z is the gapwise direction, and the

velocities in x−y plain are symmetric over a centerline, therefore, at the center, the following equations are tenable.

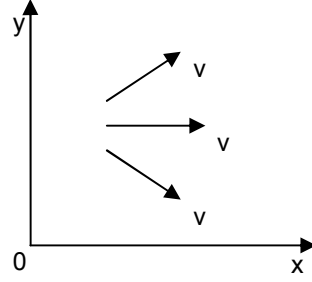$$v_y = 0, \quad v_z = 0, \quad \frac{\partial v_x}{\partial y} = 0 \tag{4-1}$$

Figure 4-1. Velocity directions of a symmetric expansion flow

4.2.1 Governing equations

The Ericksen Transversely Isotropic Fluid equations are used for modeling the motion of the director.

$$\frac{\partial v_x}{\partial x} + \frac{\partial v_y}{\partial y} = 0 \tag{4-2}$$

$$\frac{Dn_i}{Dt} = W_{ij}n_j + \lambda(A_{ij}n_j - n_i n_k n_l A_{kl}) \tag{4-3}$$

$$n_x^2 + n_y^2 + n_z^2 = 1 \tag{4-4}$$

where

$$W_{ij} = \frac{1}{2}(\frac{\partial v_i}{\partial j} - \frac{\partial v_j}{\partial i}) \tag{4-5}$$

$$A_{ij} = \frac{1}{2}(\frac{\partial v_i}{\partial j} + \frac{\partial v_j}{\partial i}) \tag{4-6}$$

$$i,j = x,y,z$$

Due to $v_y=0$ and $v_z=0$,

$$\frac{\partial v_y}{\partial x} = \frac{\partial v_y}{\partial z} = \frac{\partial v_z}{\partial x} = \frac{\partial v_z}{\partial y} = \frac{\partial v_z}{\partial z} = 0 \qquad (4\text{-}7)$$

Then :

$$\mathbf{W} = \frac{1}{2}\begin{bmatrix} 0 & 0 & \frac{\partial v_x}{\partial z} \\ 0 & 0 & 0 \\ -\frac{\partial v_x}{\partial z} & 0 & 0 \end{bmatrix} \qquad (4\text{-}8)$$

$$\mathbf{A} = \frac{1}{2}\begin{bmatrix} 2\frac{\partial v_x}{\partial x} & 0 & \frac{\partial v_x}{\partial z} \\ 0 & 2\frac{\partial v_y}{\partial y} & 0 \\ \frac{\partial v_x}{\partial z} & 0 & 0 \end{bmatrix} \qquad (4\text{-}9)$$

Equation (4-3) turns to:

$$\frac{Dn_x}{Dt} = \frac{1+\lambda}{2}\frac{\partial v_x}{\partial z}n_z + \lambda \cdot n_x(\frac{\partial v_x}{\partial x} - m) \qquad (4\text{-}10a)$$

$$\frac{Dn_y}{Dt} = \lambda \cdot n_y(\frac{\partial v_y}{\partial y} - m) \qquad (4\text{-}10b)$$

$$\frac{Dn_z}{Dt} = \frac{\lambda-1}{2}\frac{\partial v_x}{\partial z}n_x - \lambda \cdot m \cdot n_z \qquad (4\text{-}10c)$$

$$m = \frac{\partial v_x}{\partial x}n_x{}^2 + \frac{\partial v_y}{\partial y}n_y{}^2 + \frac{\partial v_x}{\partial z}n_x n_z \qquad (4\text{-}11)$$

4.2.2 Steady state analysis

At steady state of a fluid particle, $\dfrac{Dn_x}{Dt} = \dfrac{Dn_y}{Dt} = \dfrac{Dn_z}{Dt} = 0$, equation (4-10a)~(4-10c)

become:

$$\frac{1+\lambda}{2}\frac{\partial v_x}{\partial z}n_z + \lambda \cdot n_x(\frac{\partial v_x}{\partial x} - m) = 0 \tag{4-12a}$$

$$\lambda \cdot n_y(\frac{\partial v_y}{\partial y} - m) = 0 \tag{4-12b}$$

$$\frac{\lambda-1}{2}\frac{\partial v_x}{\partial z}n_x - \lambda \cdot m \cdot n_z = 0 \tag{4-12c}$$

1) When $n_y \neq 0$

Equation (4-12b) becomes

$$m = \frac{\partial v_y}{\partial y} \tag{4-13}$$

And equation (4-12a) and (4-12c) become:

$$\frac{1+\lambda}{2}\frac{\partial v_x}{\partial z}n_z + 2\lambda \frac{\partial v_x}{\partial x}n_x = 0 \tag{4-14a}$$

$$\frac{\lambda-1}{2}\frac{\partial v_x}{\partial z}n_x + \lambda \frac{\partial v_x}{\partial x}n_z = 0 \tag{4-14b}$$

The solution of the above equations is: $n_x = n_z = 0$. Obviously the point with $n_x = n_z = 0$ and $n_y = 1$ satisfies equation (4-4) and (4-12a)~(4-12c).   Therefore $n_x = n_z = 0$ and $n_y = 1$ is a balance point of director.

Let $q_1 = n_x$, $q_2 = n_z$, then at the above balance point, $q_1 = q_2 = 0$.

$$\frac{D\mathbf{q}}{Dt} = \mathbf{Q} \cdot \mathbf{q} + O(\|\mathbf{q}\|^2) \tag{4-15}$$

where

$$\mathbf{Q} = \begin{bmatrix} 2\lambda \cdot \frac{\partial v_x}{\partial x} & \frac{1}{2}\frac{\partial v_x}{\partial z}(\lambda+1) \\ \frac{1}{2}\frac{\partial v_x}{\partial z}(\lambda-1) & \lambda \cdot \frac{\partial v_x}{\partial x} \end{bmatrix} \tag{4-16}$$

The condition for local stable of equation (4-15) at **q=0** is that all the eigenvalues of **Q** have minus real part. It means all the roots of equation (4-17) should have minus real part. That requests all its coefficients are positive.

$$s^2 - 3\lambda \cdot \frac{\partial v_x}{\partial x} s + 2\lambda^2 (\frac{\partial v_x}{\partial x})^2 - \frac{1}{4}(\frac{\partial v_x}{\partial z})^2 (\lambda^2 - 1) = 0 \tag{4-17}$$

Conclusion 1: At the center of a symmetric expansion Hele-Shaw flow shown in figure 4-1, the condition for local stable of the director of a fluid particle with $n_x=n_z=0$ and $n_y=1$ is:

$$(\frac{\partial v_x}{\partial z})^2 < \frac{8\lambda^2}{\lambda^2-1}(\frac{\partial v_x}{\partial x})^2 \quad \text{and} \quad \frac{\partial v_x}{\partial x} < 0 \tag{4-18}$$

2) When $n_y=0$

Equation (4-4) becomes:

$$n_x{}^2 + n_z{}^2 = 1 \tag{4-19}$$

Obviously $n_x=n_z=0$ violates equation (4-19). Then equation (4-20) must be tenable for the solutions of equation (4-12a) and (4-12c) other than $n_x=n_z=0$.

$$4\lambda^2 m^2 - 4\lambda^2 \frac{\partial v_x}{\partial x} m - (\frac{\partial v_x}{\partial z})^2 (\lambda^2 - 1) = 0 \tag{4-20}$$

The roots are:

$$m_1 = \frac{1}{2}\frac{\partial v_x}{\partial x} + \frac{\sqrt{\lambda^2(\frac{\partial v_x}{\partial x})^2 + (\frac{\partial v_x}{\partial z})^2(\lambda^2 - 1)}}{2\lambda} \tag{4-21a}$$

and

$$m_2 = \frac{1}{2}\frac{\partial v_x}{\partial x} - \frac{\sqrt{\lambda^2(\frac{\partial v_x}{\partial x})^2 + (\frac{\partial v_x}{\partial z})^2(\lambda^2 - 1)}}{2\lambda} \tag{4-21b}$$

From equation (4-12c), (4-19), and (4-20), we can get the steady director with $n_{y0}=0$:

$$n_{x0} = \frac{\lambda \cdot m}{\sqrt{\lambda^2 m^2 + (\frac{\lambda-1}{2})^2(\frac{\partial v_x}{\partial z})^2}} \tag{4-22a}$$

$$n_{z0} = \frac{(\lambda - 1)}{2\lambda m} \frac{\partial v_x}{\partial z} n_{x0} \tag{4-22b}$$

It can be proved that this solution also satisfies equation (4-11), (4-12a), and (4-12b). Therefore, it is a balance point of the director.

Let $q_1 = n_x - n_{x0}$, $q_2 = n_y - n_{y0}$, then at balance point $q_1 = q_2 = 0$

According to $n_x^2 + n_y^2 + n_z^2 = 1$, we can get:

$$\frac{\partial n_z}{\partial n_x} = -\frac{n_x}{n_z} \quad \text{and} \quad \frac{\partial n_z}{\partial n_y} = -\frac{n_y}{n_z} \tag{4-23}$$

Then near the balance points, we have:

$$n_z = n_{z0} + \frac{\partial n_z}{\partial n_x}\bigg|_{balance-point} q_1 + \frac{\partial n_z}{\partial n_y}\bigg|_{balance-point} q_2 + o(\|\mathbf{q}\|^2) \tag{4-24}$$

Equation (4-10a) and (4-10b) turn to:

$$\frac{D\mathbf{q}}{Dt} = \mathbf{Q} \cdot \mathbf{q} + \mathbf{B} + O(\|\mathbf{q}\|^2) \tag{4-25}$$

where

$$\mathbf{Q} = \begin{bmatrix} \lambda \left(\frac{\partial v_x}{\partial x} - m\right) - \frac{\lambda+1}{2} \frac{\partial v_x}{\partial z} \frac{n_{x0}}{n_{z0}} & -\frac{\lambda+1}{2} \frac{\partial v_x}{\partial z} \frac{n_{y0}}{n_{z0}} \\ 0 & -\lambda(m + \frac{\partial v_x}{\partial x}) \end{bmatrix} \tag{4-26a}$$

$$\mathbf{B} = \begin{bmatrix} \frac{\lambda+1}{2} \frac{\partial v_x}{\partial z} n_{z0} + \lambda \left(\frac{\partial v_x}{\partial x} - m\right) n_{x0} \\ -\lambda(m + \frac{\partial v_x}{\partial x}) n_{y0} \end{bmatrix} = \mathbf{0} \tag{4-26b}$$

The local stable conditions are:

$$\lambda \; (\frac{\partial v_x}{\partial x} - m) - \frac{\lambda + 1}{2} \; \frac{\partial v_x}{\partial z} \frac{n_{x0}}{n_{z0}} \; < 0 \qquad (4\text{-}27a)$$

and

$$-\lambda(m + \frac{\partial v_x}{\partial x}) \; < 0 \qquad (4\text{-}27b)$$

Equation (4-25) is unstable for $m=m_2$. When $m=m_1$, the condition for local stable of equation (4-25) is:

$$(\frac{\partial v_x}{\partial z})^2 \; > \; \frac{8\lambda^2}{\lambda^2 - 1} (\frac{\partial v_x}{\partial x})^2 \qquad (4\text{-}28)$$

Conclusion 2: At the center of a symmetric expansion Hele-Shaw flow shown in figure 4-1, the condition for local stable of the director of a fluid particle with $n_y=0$ is equation (4-28)

4.2.3 Discussion

It can be seen from conclusion 1 and conclusion 2 that, in expansion Hele-Shaw flows of nematics, there is a singular point for the steady state of director. If the shear rate in z direction is larger than a switch value, which is a function of velocity derivatives in x-y plane, the steady director will align with the flow direction; otherwise, if the shear rate in z direction is less than the switch value, the director will tend to be perpendicular to the flow direction. In Hele-Shaw flows, there exists two this kind singular layers near the center. The position changing of the singular layers during the injection process will produce irregular director oscillations around the two singular layers. This result may help to explain a widely recognized phenomenon in the molding process of nematic polymers, which is that the molecular chains in the skin regions are largely aligned along the injection direction while the chain orientation in the central core is more or less random

In the central core between the two singular layers, there is no strong shear rate to keep the director. Therefore, the director orientation will tend to be random due to the irregular director oscillations around the two singular layers. In the skin layers, the strong shear rate in gapwise direction will guarantee the director aligning along the flow directions.

4.3 Simulation of isothermal flow

4.3.1 Introduction

At present, Leslie-Ericksen (L-E) theory and Doi's theory are the two popular constitutive theories for liquid crystals [1]. The L-E theory, which is based on macroscopic continuum mechanics, is suitable for describing the rheological properties of low molecular weight nematics. The Doi's theory, derived from microscopic molecular theory, is a kinetic model for rod-like polymers. Usually the Doi's model is too complicated to be used in the simulation of complex flows. As mentioned by Rong-Yen Chang et al in [2], Marrucci, Kuzuu and Doi have demonstrated that the Doi's theory could be reduced to the L-E theory in the limit of low shear rates. Many researchers have used the L-E theory in analyzing flow-induced behaviour of LCPs. For example, Shigeomi CHONO and Tomohiro TSUJI in [1], Rong-Yen Chang et al in [2], Marifi Guler in [3], Baleo et al in [4] and Vanderheyden and Ryskin in [5]
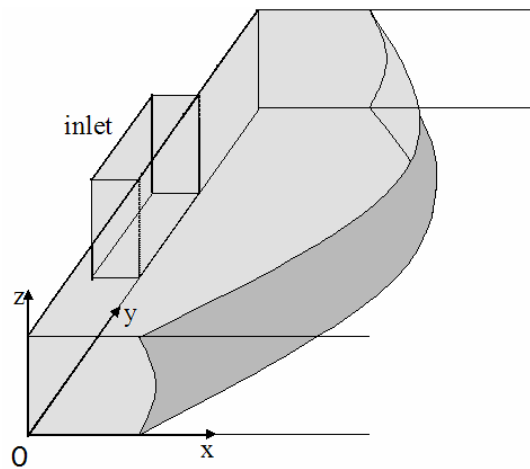
Fig 4-2. A Hele-Shaw type flow in a mould cavity

This simulation focuses on the LCPs flows during injection moulding in thin-walled moulds, as shown in figure 4-2. These flow fields can be approximated as Hele-Shaw flows in which one dimension (z direction) is much smaller in comparison with the other two. As demonstrated by M. Cengiz Altan et al in [8], this physical feature allows for following simplifications: (1) viscous forces are dominant, and inertial forces can be neglected in the momentum equations. (2) flow and dynamics forces in the gapwise direction can be neglected. (3) shear stresses through the gapwidth are dominant and the in-plane stresses can be neglected. It means that the shear rates through the gapwidth are

dominant and the in-plane shear rates can be neglected. (4) the fluid is assumed incompressible.

4.3.2 Governing equations

As pointed out by W.B. Vanderheyden and G. Ryskin in [5], LCPs exhibit very high viscosities and it is reasonable to use the high viscosity approximation in LCPs flows.

The Ericksen-Leslie equations of motion in the high viscosity limit are given by:

Continuity equation:

$$\nabla \cdot \mathbf{v} = 0 \tag{4-29}$$

Momentum equation:

$$-\nabla p + \nabla \cdot \boldsymbol{\tau} = \mathbf{0} \tag{4-30}$$

Angular momentum equation:

$$\frac{D\mathbf{n}}{Dt} = \mathbf{W} \cdot \mathbf{n} + \lambda(\mathbf{A} \cdot \mathbf{n} - \mathbf{n} \cdot \mathbf{A} \cdot \mathbf{nn}) \tag{4-31}$$

The stress tensor:

$$\boldsymbol{\tau} = \beta_0 \mathbf{A} + \beta_1 \mathbf{n} \cdot \mathbf{A} \cdot \mathbf{nnn} + \beta_2 (\mathbf{nn} \cdot \mathbf{A} + \mathbf{A} \cdot \mathbf{nn}) \tag{4-32}$$

where $\mathbf{v}$ is velocity vector, p is pressure, $\mathbf{n}$ is the director orientation vector, $\boldsymbol{\tau}$ is the stress tensor, $\mathbf{A}$ is the rate of strain tensor:

$$\mathbf{A} = \frac{(\nabla \mathbf{v})^T + \nabla \mathbf{v}}{2} \tag{4-33}$$

and $\mathbf{W}$ is the vorticity tensor:

$$\mathbf{W} = \frac{\nabla \mathbf{v} - (\nabla \mathbf{v})^T}{2} \tag{4-34}$$

According to Hele-Shaw approximations, the momentum equation (4-30) can be written as:

in x direction:

$$\frac{\partial p(x,y)}{\partial x} = \frac{\partial \tau_{zx}(x,y,z)}{\partial z} \qquad (4\text{-}35a)$$

in y direction:

$$\frac{\partial p(x,y)}{\partial y} = \frac{\partial \tau_{zy}(x,y,z)}{\partial z} \qquad (4\text{-}35b)$$

and the angular momentum equation (4-31) can be written as:

$$\frac{\partial n_x}{\partial t} + v_x \frac{\partial n_x}{\partial x} + v_y \frac{\partial n_x}{\partial y} = \frac{(1+\lambda)}{2} \frac{\partial v_x}{\partial z} n_z - \lambda n_x q_1 \qquad (4\text{-}36a)$$

$$\frac{\partial n_y}{\partial t} + v_x \frac{\partial n_y}{\partial x} + v_y \frac{\partial n_y}{\partial y} = \frac{(1+\lambda)}{2} \frac{\partial v_y}{\partial z} n_z - \lambda n_y q_1 \qquad (4\text{-}36b)$$

$$\frac{\partial n_z}{\partial t} + v_x \frac{\partial n_z}{\partial x} + v_y \frac{\partial n_z}{\partial y} = -\lambda n_z q_1 - (n_x \frac{\partial v_x}{\partial z} + n_y \frac{\partial v_y}{\partial z}) \frac{1-\lambda}{2} \qquad (4\text{-}36c)$$

where

$$q_1 = n_z (n_x \frac{\partial v_x}{\partial z} + n_y \frac{\partial v_y}{\partial z}) \qquad (4\text{-}37)$$

In equation (4-36a)~(4-36c), the partial derivatives of velocities on x and y are neglected according to Hele-Shaw approximation. However, these terms are kept in the central core due to the fact that the shear rate in z direction is zero in the central plane and the director orientations in the central core are mainly determined by the shear rates in x-y plane.

From the stress tensor equation (4-32) we can get:

$$\tau_{zx} = f_1(x,y,z) \frac{\partial v_x}{\partial z} + f_2(x,y,z) \frac{\partial v_y}{\partial z} \qquad (4\text{-}38a)$$

$$\tau_{zy} = f_2(x,y,z) \frac{\partial v_x}{\partial z} + f_3(x,y,z) \frac{\partial v_y}{\partial z} \qquad (4\text{-}38b)$$

where

$$f_1(x,y,z) = \frac{\beta_0}{2} + \beta_1 \cdot n_x^{\,2} n_z^{\,2} + \frac{\beta_2}{2}(n_x^{\,2} + n_z^{\,2}) \qquad (4\text{-}39a)$$

$$f_2(x, y, z) = n_x n_y (\beta_1 \cdot n_z{}^2 + \frac{\beta_2}{2}) \tag{4-39b}$$

$$f_3(x, y, z) = \frac{\beta_0}{2} + \beta_1 \cdot n_y{}^2 n_z{}^2 + \frac{\beta_2}{2}(n_y{}^2 + n_z{}^2) \tag{4-39c}$$

By substituting the stress tensor equations into the momentum equations and integrating the momentum equations in z direction twice, the velocities in term of pressure difference can be derived as:

$$v_x = \frac{\partial p}{\partial x} \int_0^z \frac{f_3}{D} z' dz' - \frac{\partial p}{\partial y} \int_0^z \frac{f_2}{D} z' dz' + C_1 \int_0^z \frac{f_3}{D} dz' - C_2 \int_0^z \frac{f_2}{D} dz' \tag{4-40a}$$

$$v_y = -\frac{\partial p}{\partial x} \int_0^z \frac{f_2}{D} z' dz' + \frac{\partial p}{\partial y} \int_0^z \frac{f_1}{D} z' dz' - C_1 \int_0^z \frac{f_2}{D} dz' + C_2 \int_0^z \frac{f_1}{D} dz' \tag{4-40b}$$

where

$$D = f_1 \cdot f_3 - (f_2)^2 \tag{4-41a}$$

$$C_1 = E_1 \frac{\partial p}{\partial x} + E_2 \frac{\partial p}{\partial y} \tag{4-41b}$$

$$C_2 = E_3 \frac{\partial p}{\partial x} + E_4 \frac{\partial p}{\partial y} \tag{4-41c}$$

$$E_1 = \frac{R_{20}R_{21} - R_{10}R_{31}}{R_{10}R_{30} - R_{20}{}^2} \tag{4-41d}$$

$$E_2 = \frac{R_{10}R_{21} - R_{20}R_{11}}{R_{10}R_{30} - R_{20}{}^2} \tag{4-41e}$$

$$E_3 = \frac{R_{30}R_{21} - R_{20}R_{31}}{R_{10}R_{30} - R_{20}{}^2} \tag{4-41f}$$

$$E_4 = \frac{R_{20}R_{21} - R_{11}R_{30}}{R_{10}R_{30} - R_{20}{}^2} \tag{4-41g}$$

$$R_{ij} = \int_0^h \frac{f_i z^j}{D} dz \tag{4-41h}$$

The approximate continuity equation of Hele-Shaw flows can be written as:

$$\frac{\partial(2h\overline{v}_x)}{\partial x} + \frac{\partial(2h\overline{v}_y)}{\partial y} = 0 \qquad (4\text{-}42)$$

where $\overline{v}_x$ and $\overline{v}_y$ stand for the averages of velocity v_x and v_y on gapwidth.

Then we can obtain the final elliptic pressure equation

$$G_1 \frac{\partial^2 p}{\partial x^2} + (G_2 + G_3)\frac{\partial^2 p}{\partial x \partial y} + G_4 \frac{\partial^2 p}{\partial y^2} + \left(\frac{\partial G_1}{\partial x} + \frac{\partial G_3}{\partial y}\right)\frac{\partial p}{\partial x}$$

$$+ \left(\frac{\partial G_2}{\partial x} + \frac{\partial G_4}{\partial y}\right)\frac{\partial p}{\partial y} = 0 \qquad (4\text{-}43)$$

where

$$G_1 = S_{31} + E_1 S_{30} - E_3 S_{20} \qquad (4\text{-}44a)$$

$$G_2 = -S_{21} + E_2 S_{30} - E_4 S_{20} \qquad (4\text{-}44b)$$

$$G_3 = -S_{21} - E_1 S_{20} + E_3 S_{10} \qquad (4\text{-}44c)$$

$$G_4 = S_{11} - E_2 S_{20} + E_4 S_{10} \qquad (4\text{-}44d)$$

$$S_{ij} = \int_0^h \frac{f_i z^j}{D}(h - z)dz \qquad (4\text{-}44e)$$

The derived pressure equation was solved by finite difference method. And a new kind of characteristic line integration method was used in solving the angular momentum equations.
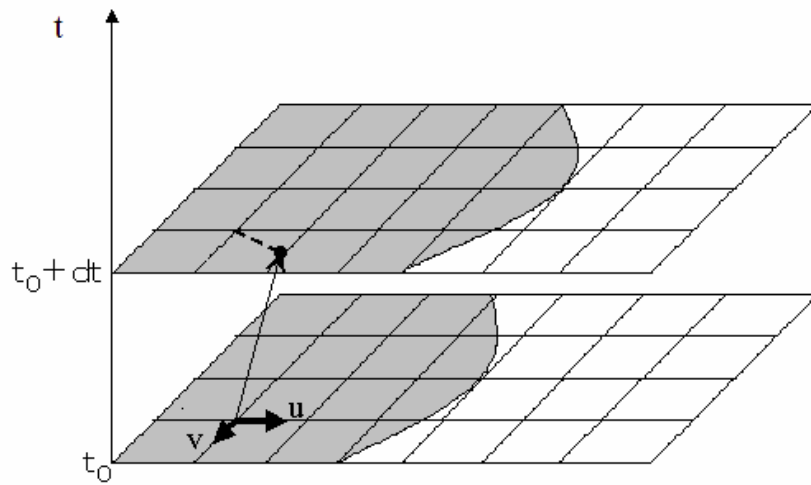
Fig 4-3. A characteristic line
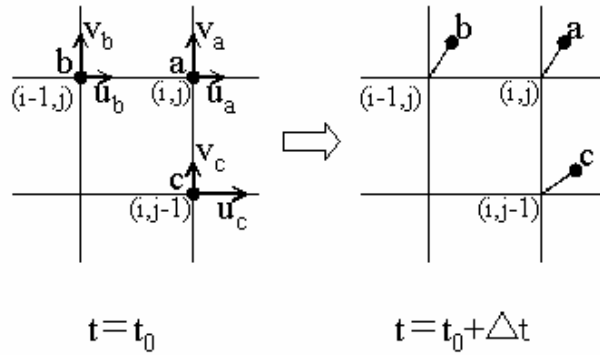
Fig 4-4. Three characteristic lines for flow particles a, b, and c which locate at grid points at time t=t_0

4.3.3 Characteristic Line Integration

Characteristic lines are the moving traces of flow particles. The dotted line in figure 4-3 is a small segment of a characteristic line which starts from a grid point at time t_0 and ends at t_0+dt. For small dt, it is reasonable to assume that the small segment of a characteristic line is straight.

There are three steps to precede the characteristic line integration on director calculation. First, at each time step, the next time step directors of the flow particles which locate at grid points at this time step are calculated by integrating the right side of the angular momentum equation at every grid points in the flow domain. Second, the positions of these flow particles at next time step are obtained by integrating along the characteristics lines passing grid points. Finally, the next time step directors of flow particles at grid points are calculated by interpolation method.

The step one is straightforward. Here is an example for step two and step three. As shown in figure 4-4, a, b, and c are three flow particles which locate at grid points at time t=t_0. Assume the coordinate of grid point (i,j) is (0,0), then at t= t_0+Δt, the position of flow particle a is ($u_a\Delta t$, $v_a\Delta t$); the position of flow particle b is ($u_b\Delta t-\Delta x$, $v_b\Delta t$); the position of flow particle c is ($u_c\Delta t$, $v_c\Delta t-\Delta y$), where Δx and Δy are grid sizes. Then by linear interpolation, the director of the flow particle at grid point (i,j) at t= t_0+Δt can be written as:

$$\mathbf{n}_{(i,j)}\Big|_{t_0+\Delta t}=c_1\mathbf{n}_a\Big|_{t_0+\Delta t}+c_2\mathbf{n}_b\Big|_{t_0+\Delta t}+c_3\mathbf{n}_c\Big|_{t_0+\Delta t} \qquad (4\text{-}45)$$

where

$$c_1 = [\mathbf{Q}^{-1}]_{(3,1)} \qquad (4\text{-}46a)$$

$$c_2 = [\mathbf{Q}^{-1}]_{(3,2)} \qquad (4\text{-}46b)$$

$$c_3 = [\mathbf{Q}^{-1}]_{(3,3)} \qquad (4\text{-}46c)$$

$$\mathbf{Q} = \begin{bmatrix} u_a\Delta t & v_a\Delta t & 1 \\ u_b\Delta t - \Delta x & v_b\Delta t & 1 \\ u_c\Delta t & v_c\Delta t - \Delta y & 1 \end{bmatrix} \qquad (4\text{-}46d)$$

4.3.4 Results and discussion

In this section, the simulation results for two mould cavities with constant inlet pressure, which are shown in figure 4-5, are presented. The Leslie viscosities used in the simulations are a set of parameters for poly (1,4-phenylene-2, 6-benzobisthiazole) estimated by Se and Berry, which are shown in table 1 (cited from [9]).

Leslie viscosities (poise)	
α_1	-5052
α_2	-2636
α_3	-439
α_4	1889
α_5	2725
α_6	-350

Table 1. Parameters used in the simulations

The coefficients used in the governing equations are given by:

$$\lambda = -\frac{\alpha_6 - \alpha_5}{\alpha_3 - \alpha_2} \tag{4-47a}$$

$$\beta_0 = \alpha_4 \tag{4-47b}$$

$$\beta_1 = \alpha_1 - \lambda(\alpha_2 + \alpha_3) \tag{4-47c}$$

$$\beta_2 = \alpha_5 + \lambda\alpha_2 \tag{4-47d}$$

The shape of the first mould cavity is approximately 7 cm wide, 8 cm long and has a gapwidth of 1 mm. Figure 4-6 shows the locations of the free surface at various times during the filling operations of the first mould cavity. The filling time is approximately 70.72 seconds. The pressure distribution near the completion of the filling stage is shown in figure 4-7. Figure 4-8 shows the flow directions near the completion of the filling stage. The director orientation distributions in the skin layers and the central core are displayed in figure 4-9 and figure 4-10.

The shape of the second mould cavity is approximately 7 cm wide, 10 cm long and has a gapwidth of 1 mm. The results of simulation for the second mould cavity are shown in figure 4-11 to figure 4-15. The filling time is approximately 108.23 seconds. It can be seen that the director orientation distributions in the central core plane and the plane near the mould wall are quite different. The director orientations in the skin regions are largely aligned along the injection directions while the director orientations in the core centre are more complicated. The high molecule orientation in the skin layer is induced by the large shear rate in gapwise direction near the wall, which tend to keep the director of LCPs align along the flow direction. In Hele-Shaw flow, this effect dominates in the skin layers. In the core centre, the shear rate in gapwise direction is zero, and the director orientations are determined by shear rates in x-y plane. Therefore, in the core centre, the injection flows are two-dimension flows in x-y plane. In case of contraction flows, the director orientations tend to be parallel to the flow directions. And in case of expansion flows, the director orientations tend to be perpendicular to the flow directions. These tendencies are disturbed by the convective term in the momentum equations and produced rather complicated results which are shown in figure 4-10 and figure 4-14.

The relations between filling time and inlet pressure for the two moulds are shown in figure 4-16. It seems that this relation can be described by equation (4-48).

$$p \cdot t_f = c \qquad\qquad (4\text{-}48)$$

where p is inlet pressure, t_f is filling time, and c is a constant.

Similarly, as show in figure 4-17, the relations between filling time and gap size fit equation (4-49) very well.

$$h^2 \cdot t_f = c \qquad\qquad (4\text{-}49)$$

where h is the gap size.

4.3.5 Conclusion

In this section, a numeric simulation approach of injection moulding process of LCPs is presented. This technique can predict the locations of melt front at selected time steps during the injection and the director orientations distributions at various time steps. The LCPs flows are modelled by Leslie-Ericken equations of motion in high viscosity limit．An elliptic pressure equation are derived under Hele-Shaw approximations. The Angular Momentum Equation was solved by a new kind of characteristic integration method.

According to Choy et al ([10]), it is widely recognized that injection-moulded plaques of liquid crystalline polymers consist mainly of two skin layers and a central core in between. The molecular chains in the skin regions are largely aligned along the injection direction while the chain orientation in the central core is more or less random. The simulation results presented in this section are consisted with this conclusion very well.

According the simulation results, the filling time is in reverse proportion to inlet pressure and in reverse proportion to the square of gap size. Further work is necessary to verify this result.
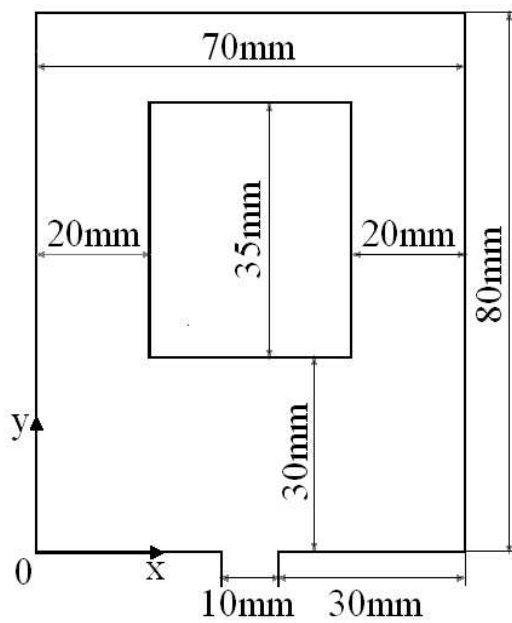
(a) geometry one
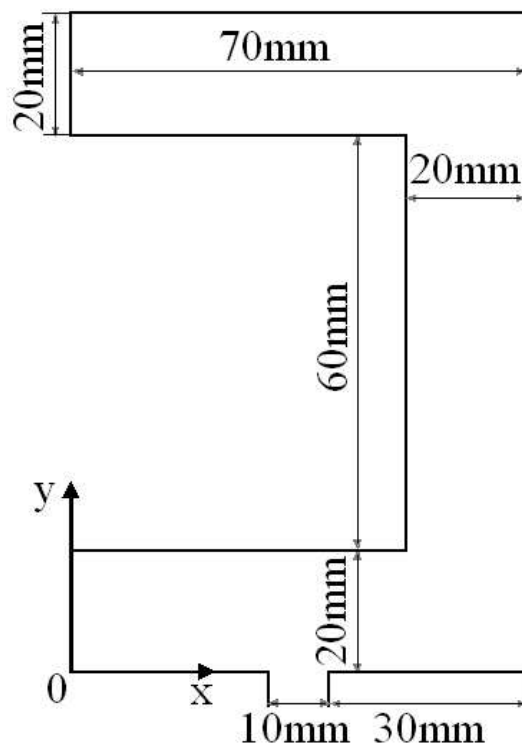
(b) geometry two

Fig 4-5 Simulation geometries
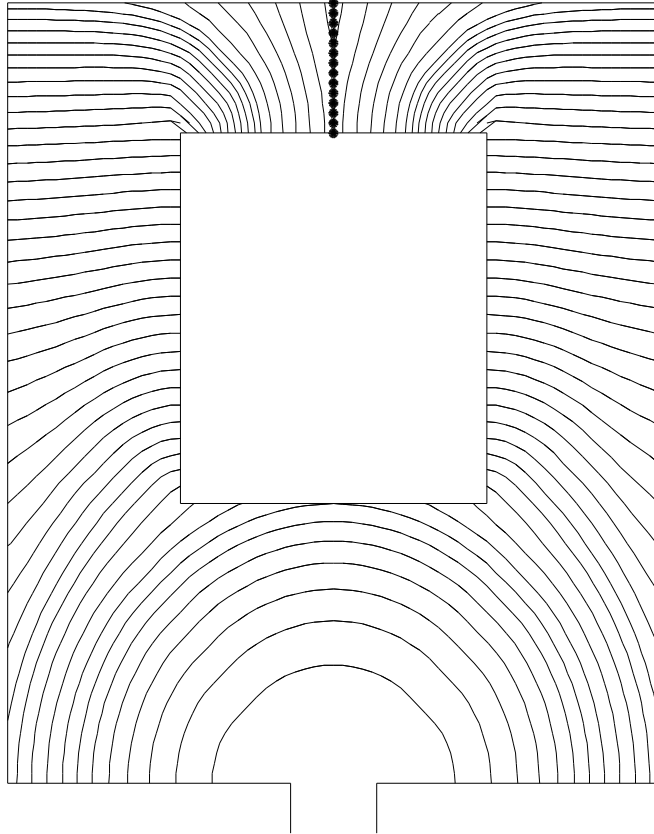
Fig 4-6 Geometry one: development of free surface, time interval= 1.5 second
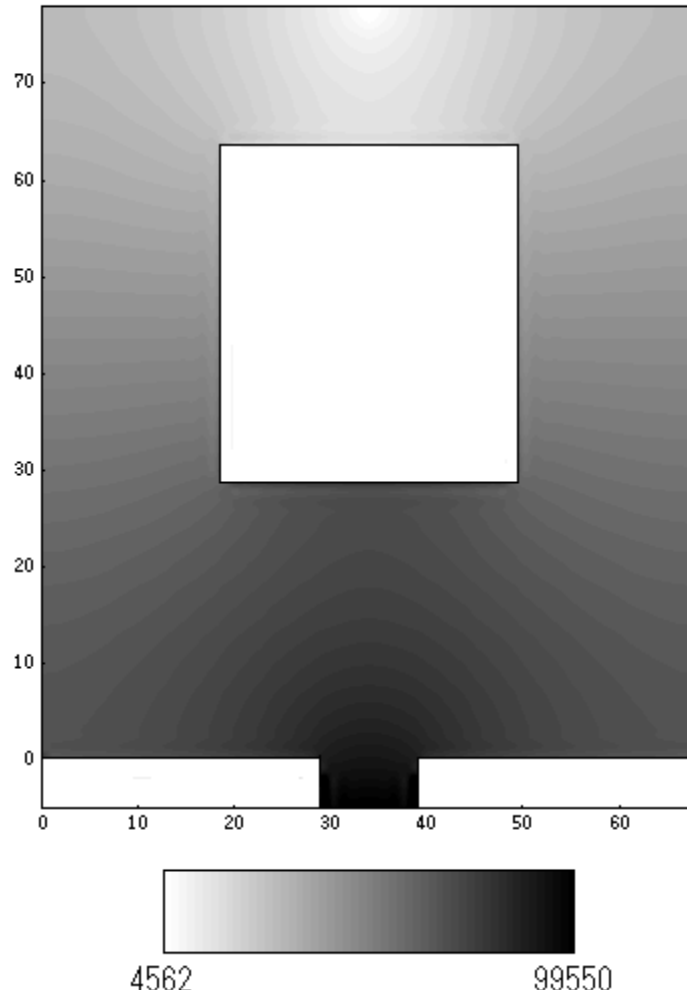
Fig 4-7. Geometry one: pressure distribution (Pa)
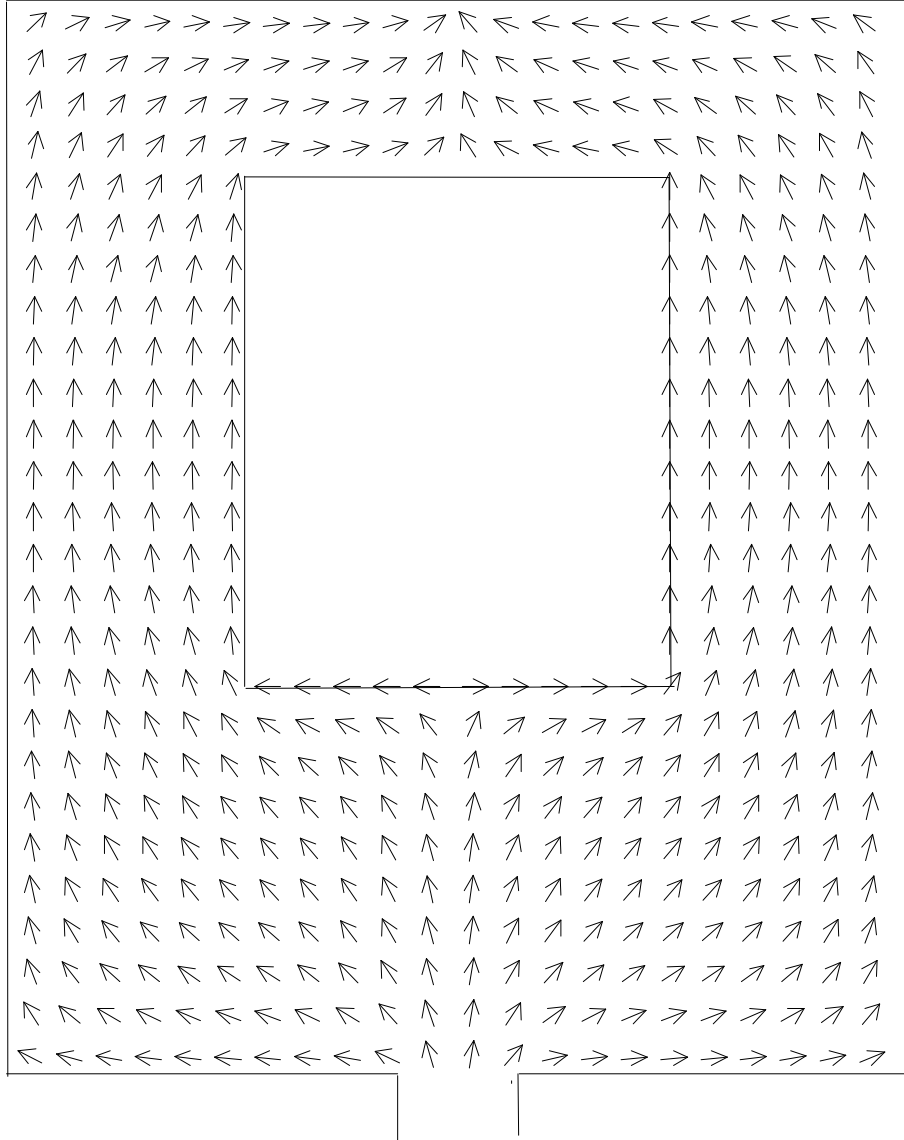
Fig 4-8. Geometry one: flow directions

40
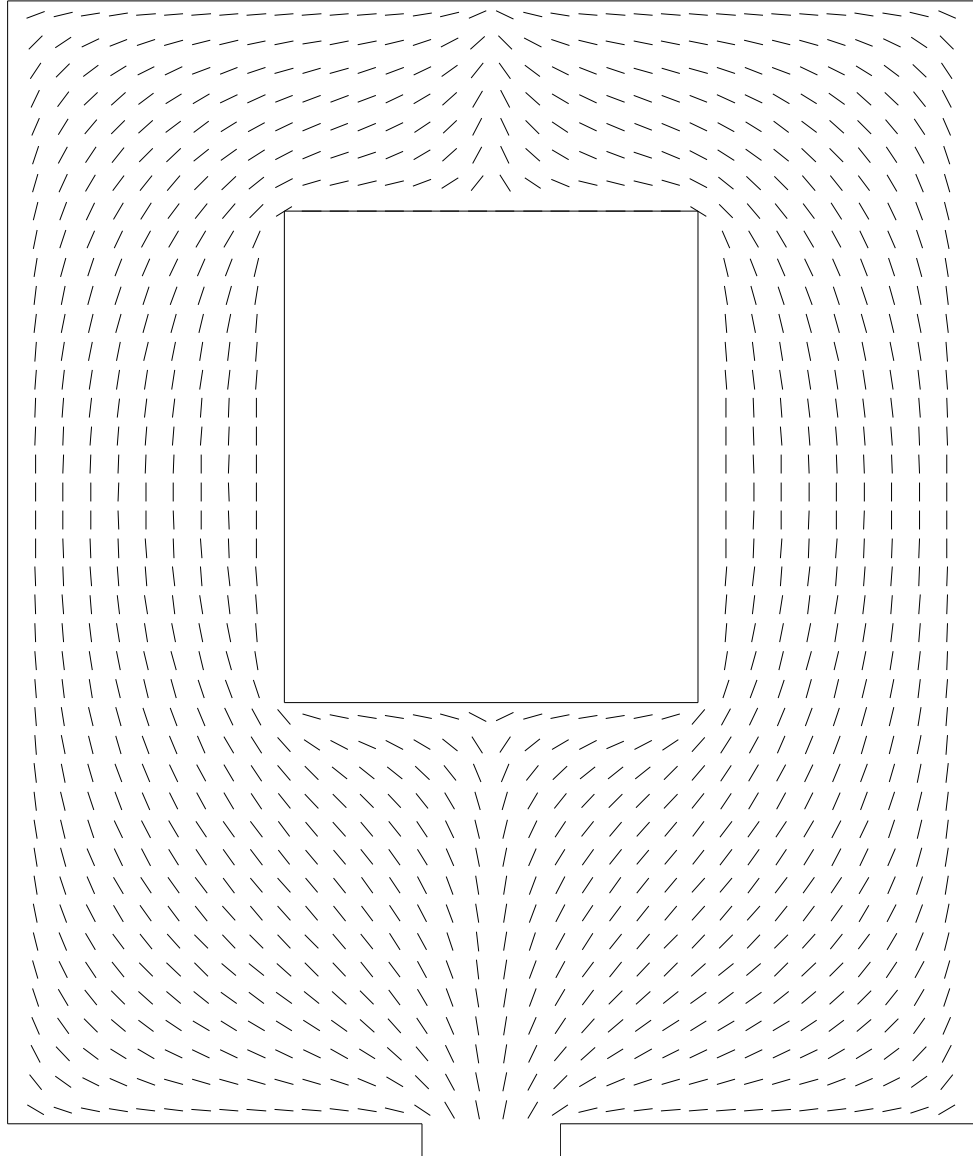
Fig 4-9. Geometry one: director orientations in skin layers
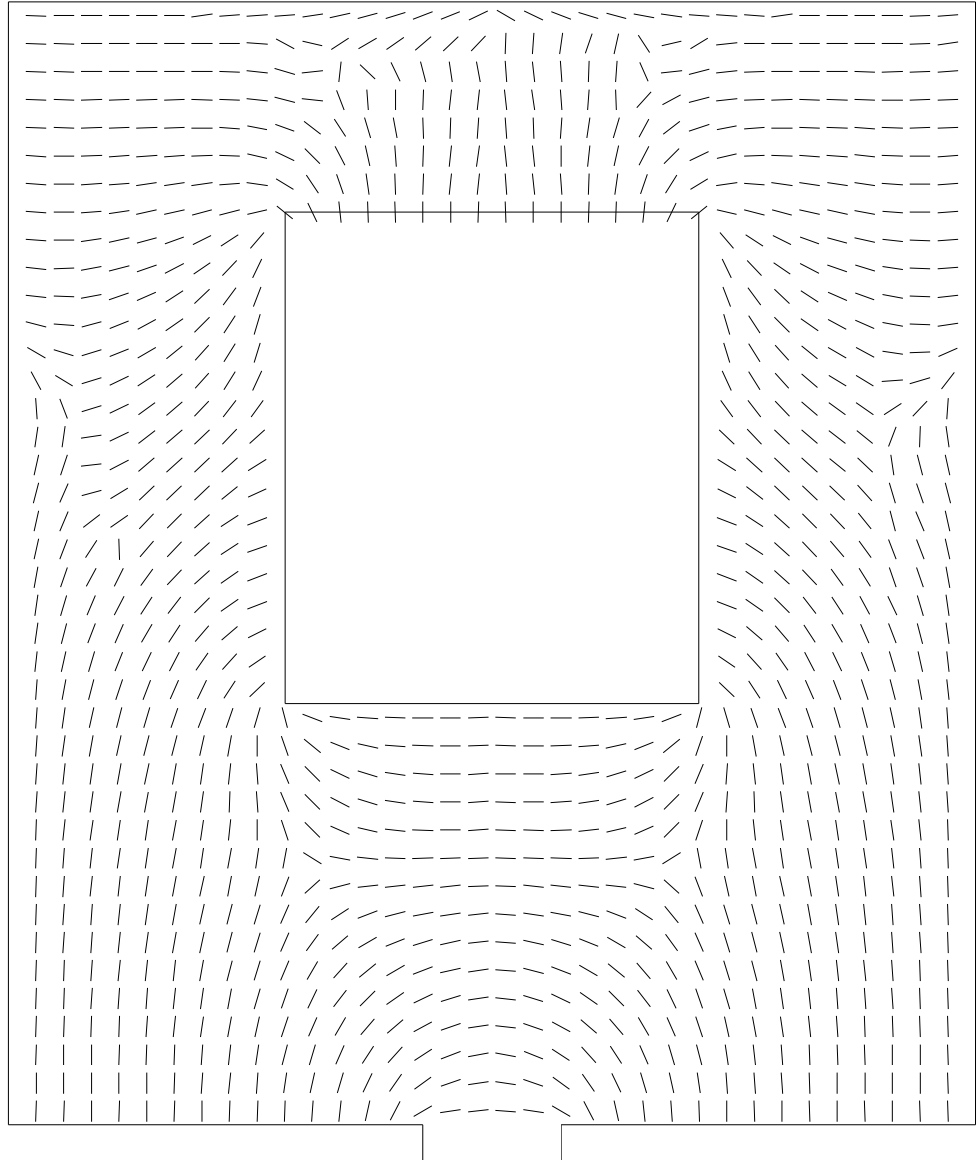
Fig 4-10 Geometry one: director orientations in central core
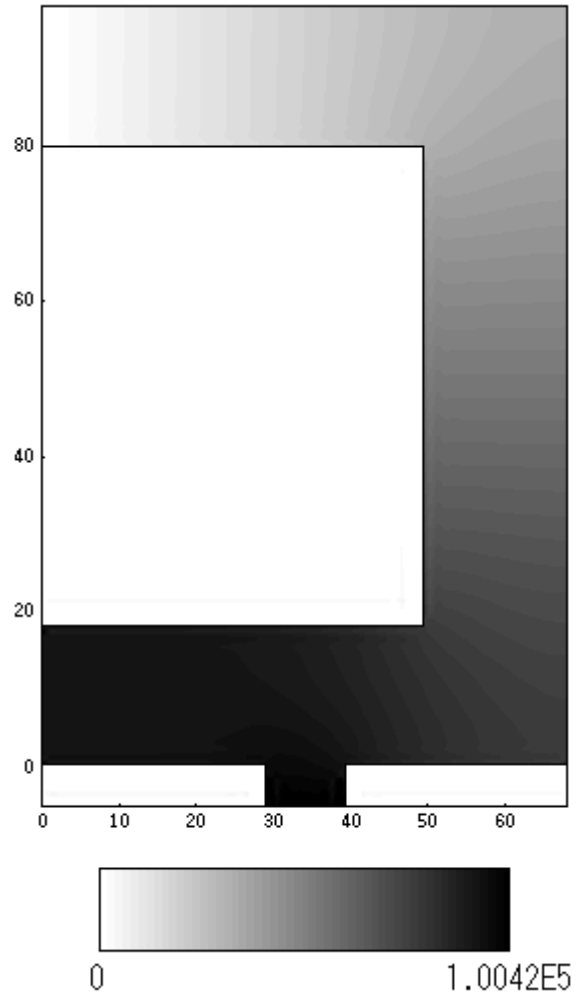
Fig 4-11. Geometry two: pressure distribution (Pa)
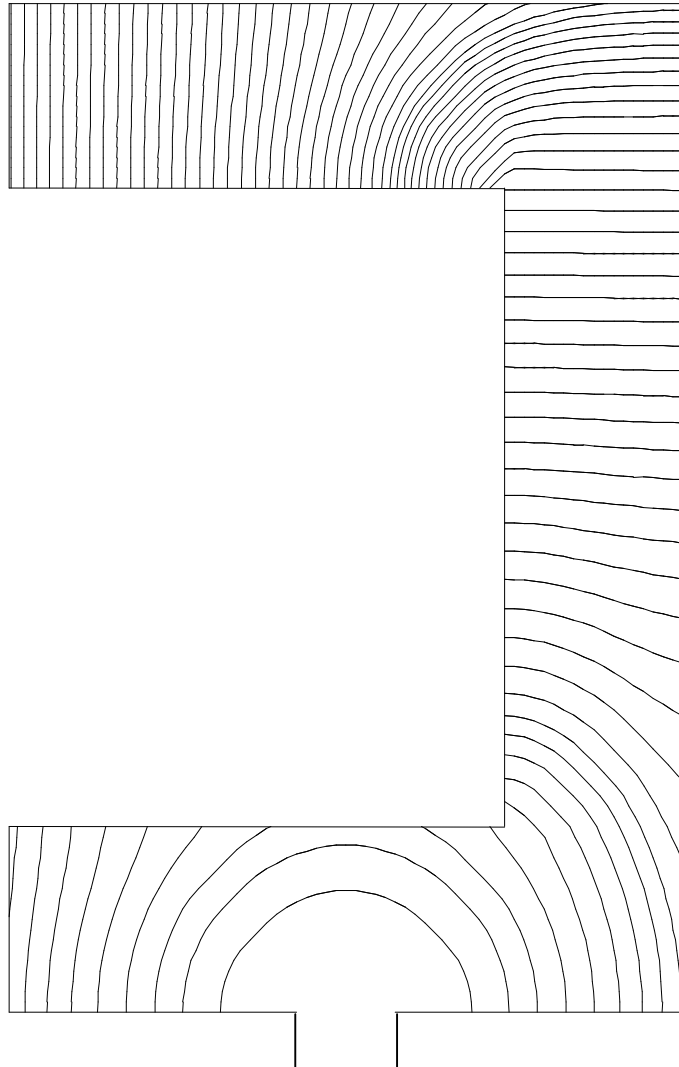
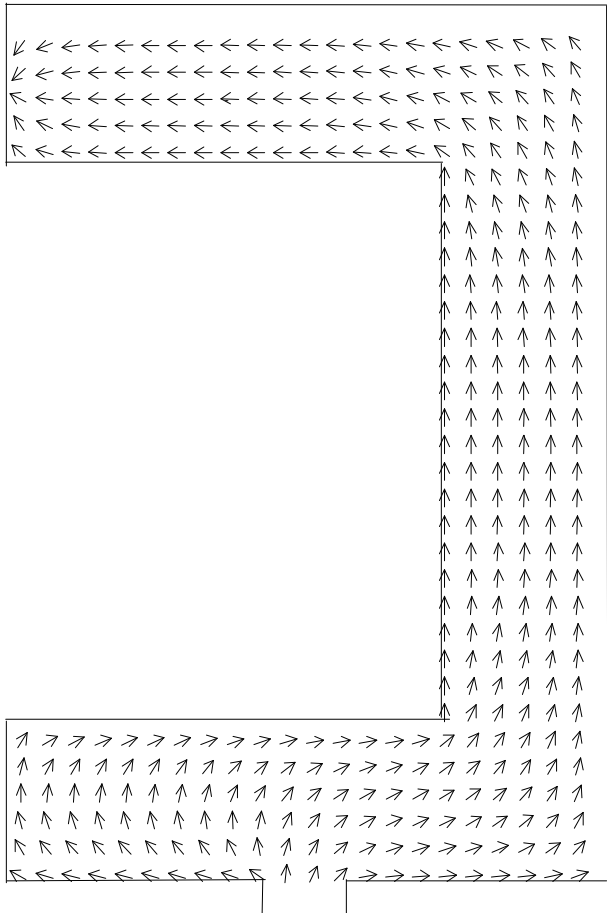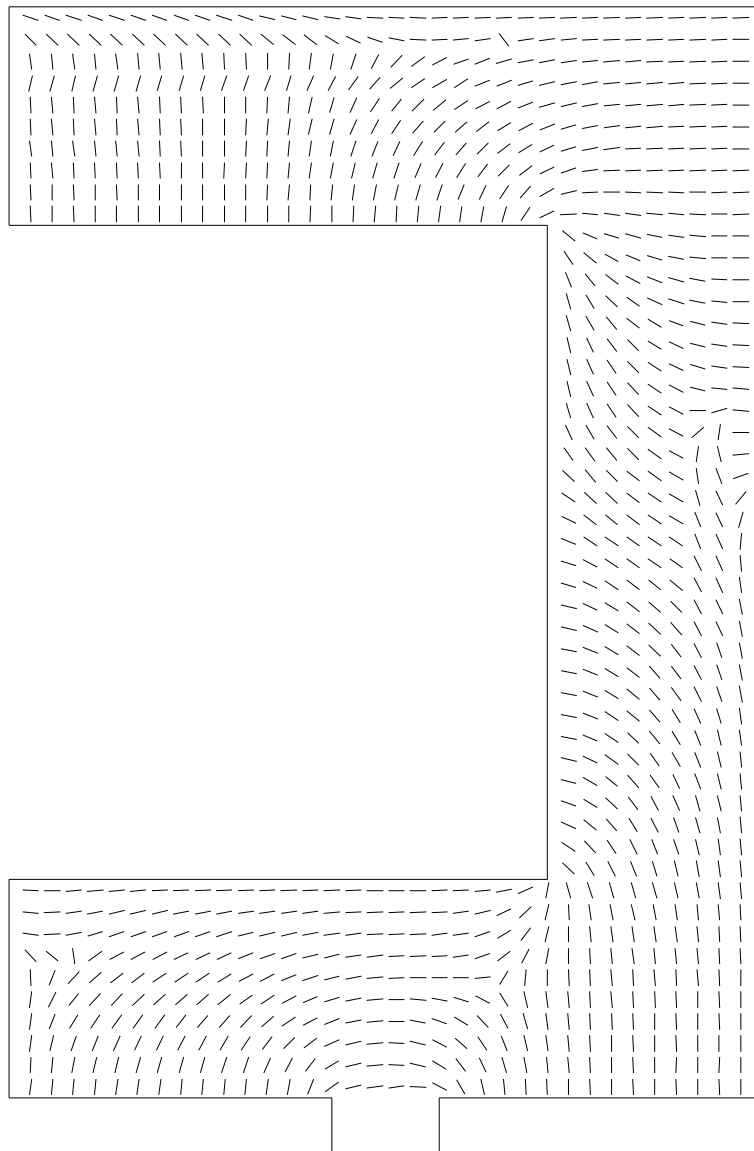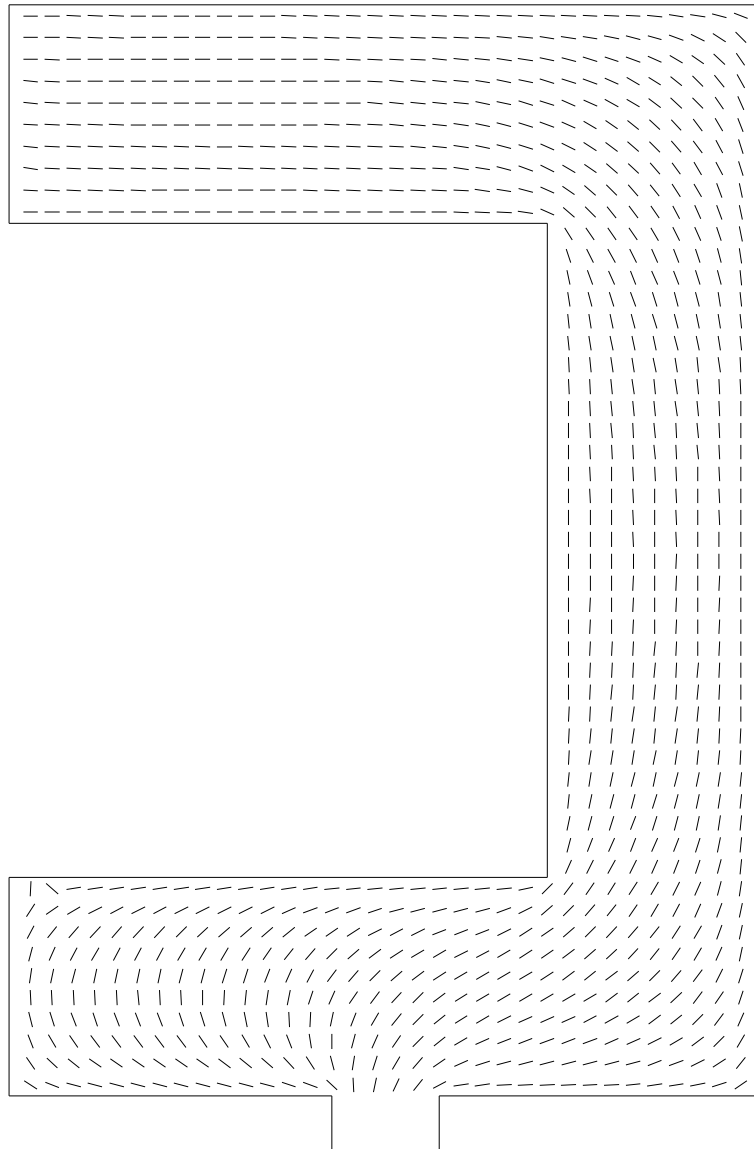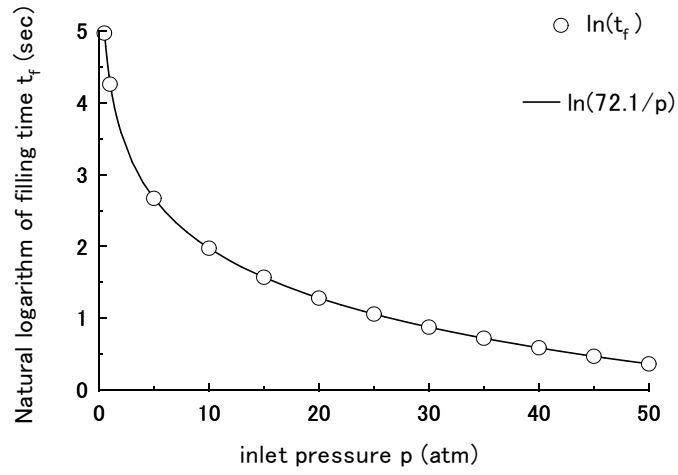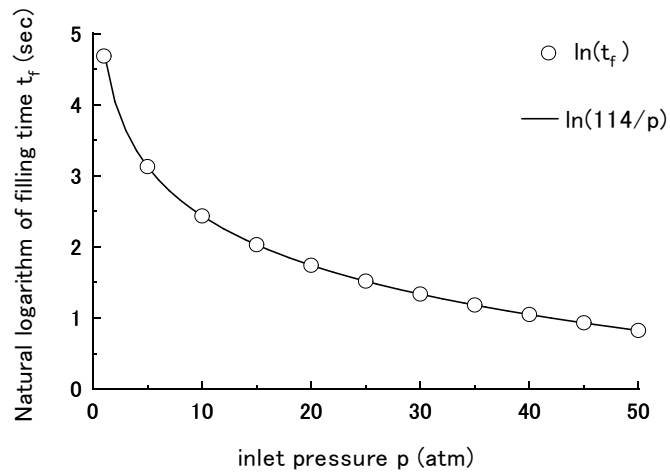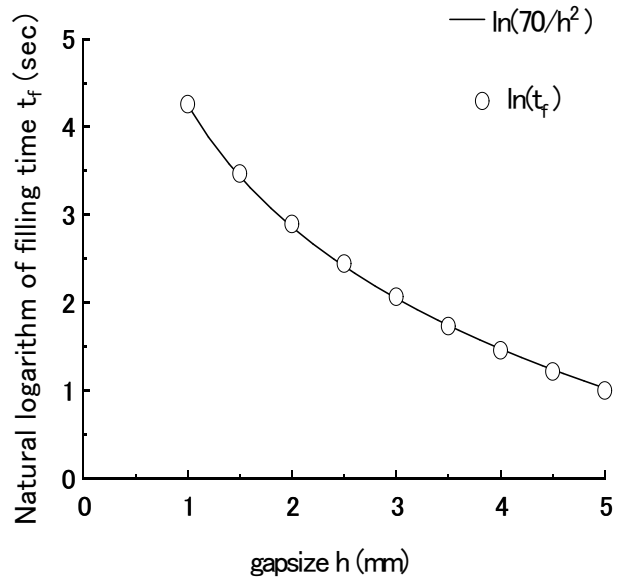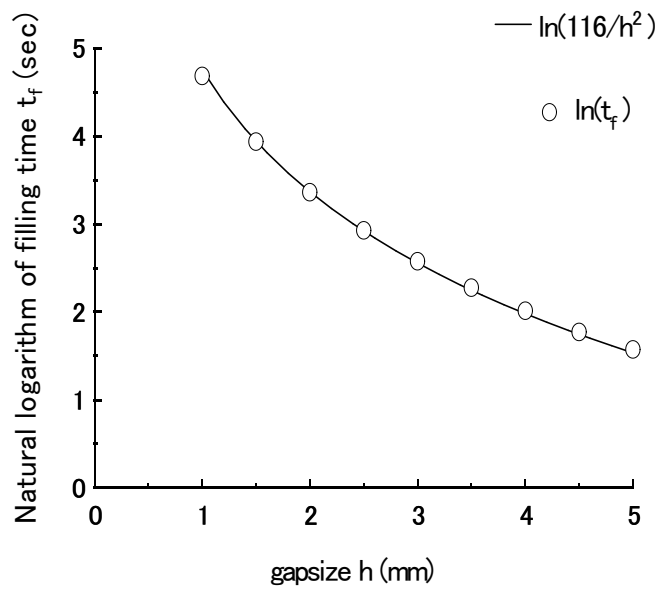Fig 4-12. Geometry two: development of free surface, time interval= 1.5 sec

Fig 4-13. Geometry two: flow directions

Fig 4-14. Geometry two: director orientations in central core

Fig 4-15. Geometry two: director orientations in skin layers

(a) geometry one

(b) geometry two

Fig 4-16. Relations between filling time and inlet pressure

(a) geometry one

(b) geometry two

Fig 4-17. Relations between filling time and gapsize

4.4 Simulation of non-isothermal flows

Non-isothermal flows of liquid crystalline polymers into two-dimensional thin cavity moulds of regular shape are simulated in this section. The flows are modelled by the governing equations obtained in section 4.3. The non-isothermal natures of the flow are modelled by the energy equation shown in section 4.4.2.

4.4.1 Viscosities

In non-isothermal flows of LCPs, the six Leslie viscosities are functions of temperature. They are given by R.G. Larson in [11] as:

$$\alpha_1 = -2\eta R^2(p)S_4 \tag{4-50a}$$

$$\alpha_2 = -\eta R(p)(1+\frac{1}{\lambda})S_2 \tag{4-50b}$$

$$\alpha_3 = -\eta R(p)(1-\frac{1}{\lambda})S_2 \tag{4-50c}$$

$$\alpha_4 = \eta R^2(p)\frac{2}{35}(7-5S_2-2S_4)+\alpha_0 \tag{4-50d}$$

$$\alpha_5 = \eta R(p)[\frac{1}{7}R(p)(3S_2+4S_4)+S_2] \tag{4-50e}$$

$$\alpha_6 = \eta R(p)[\frac{1}{7}R(p)(3S_2+4S_4)-S_2] \tag{4-50f}$$

where η is the characteristic viscosity, S_2 and S_4 are the second and fourth moments of the molecule distribution function, $R(p)$ is a parameter that depends on the effective aspect ratio p of the rigid molecules.

$$R(p)=\frac{p^2-1}{p^2+1} \tag{4-51}$$

The term α_0 was added to the theory by Larson and Archer(1995) to account phenomenologically for contribution to momentum transport other than those due to rotational motions. It is expected to be negligible for polymeric nematics.

The second and fourth moments S_2 and S_4, whose Maier-Saupe values are shown in table 2, can be predicted by the simple Maier-Saupe theory ([11]).

T/T_{NI}	S_2	S_4
0.999	0.441	0.127
0.990	0.471	0.145
0.985	0.485	0.154
0.975	0.509	0.171
0.965	0.530	0.186
0.955	0.549	0.200
0.945	0.566	0.213
0.930	0.588	0.232
0.920	0.602	0.244
0.910	0.615	0.256
0.900	0.627	0.268
0.880	0.649	0.290
0.860	0.669	0.311
0.840	0.687	0.331
0.800	0.719	0.370
0.715	0.772	0.446
0.505	0.864	0.619
0.303	0.926	0.775

Table 2. S_2 and S_4 from the Maier-Saupe Theory

The tumbling parameter λ can be obtained by the following simple approximation form (Stepanov 1983; Kroger and Sellers 1995; Archer and Larson 1995) ([11]):

$$\lambda = R(p)\frac{5S_2 + 16S_4 + 14}{35S_2} \tag{4-52}$$

The characteristic viscosity η can be obtained from fits to the viscosity data of the liquid at temperature above T_{NI}, at which the liquid is in the isotropic state and has no orientational order, so that $S_2=S_4=0$. Then the Newtonian viscosity η_{iso} of this isotropic liquid is given by:

$$\eta_{iso} = \frac{\alpha_4}{2} = \frac{\eta}{5} \tag{4-53}$$

Shenoy and Saint measured the viscosity of liquid crystalline melts of copolymers of ethylene terephthalate (ETP) and p-hydroxy benzoic acid (HBA) in a range of shear rates and temperatures and at different polymer compositions. Their data for the 60

mol% HBA : 40 mol% ETP composition have been fitted by C. Lekakou in [6]. The result of C. Lekahou which is shown in equation (4-54) was used as η_{iso} in this study.

$$\eta_{iso} = 8.18 \times 10^{-4} \dot{\gamma}^{0.82-1} e^{6752/T} \tag{4-54}$$

4.4.2 Energy equation

The energy equation for uncompressible LCPs can be written as:

$$\rho C_v \frac{DT}{Dt} = (\nabla \cdot \mathbf{q}) + (\boldsymbol{\tau} : \nabla \mathbf{v}) \tag{4-55}$$

where ρ is density, C_v is heat capacity per unit mass, $\mathbf{q}$ is the heat flow, T is temperature, and $\boldsymbol{\tau}$ is stress tensor.

The heat flow $\mathbf{q}$ for LCPs is given by:

$$\mathbf{q} = \beta_{t1}(\mathbf{n} \cdot \nabla T)\mathbf{n} + \beta_{t2}\nabla T \tag{4-56}$$

where β_{t1} and β_{t2} are thermal conductivity coefficients with β_{t1} expressing the anisotropy ([12]).

In Hele-Shaw flow, we can assume that the heat conductions in gapwise direction are dominant and the in-plane heat conductions can be neglected. The energy equation can be simplified as

$$\rho C_v \frac{DT}{Dt} = \alpha \frac{\partial^2 T}{\partial z^2} + \beta \frac{\partial T}{\partial z} + \beta_{t1} n_z n_x \frac{\partial^2 T}{\partial x \partial z} + \beta_{t1} n_z n_y \frac{\partial^2 T}{\partial y \partial z} + (\tau : \nabla \mathbf{v}) \tag{4-57}$$

where

$$\alpha = \beta_{t1} n_z^{\ 2} + \beta_{t2} \tag{4-58a}$$

$$\beta = \beta_{t1} n_z \left(\frac{\partial n_x}{\partial x} + \frac{\partial n_y}{\partial y} + 2 \frac{\partial n_z}{\partial z} \right) + \beta_{t1} \left(n_x \frac{\partial n_z}{\partial x} + n_y \frac{\partial n_z}{\partial y} \right) \tag{4-58b}$$
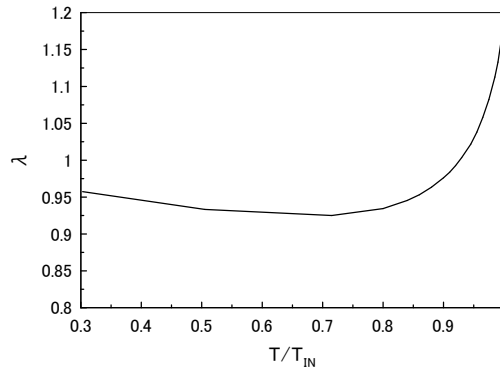
Fig 4-18. The relation between tumbling parameter λ and T/T_{IN}

4.4.3 Results and discussion

In this section, the simulation results of the injection moulding of LCPs with constant inlet pressure are presented. The melt was considered to enter the cavity at an inlet temperature of 300°C. A constant inlet pressure of 60 atmospheric pressures was assumed during the filling stage.

The shape of the first mould cavity is approximately 7 cm wide, 8 cm long and has a gapwidth of 3 mm.

The simulation results when the mould wall was held at a constant temperature of 150°C were displayed in figure 4-19 to figure 4-22. Figure 4-19 shows the locations of the free surface at various times during the filling operations. The filling time is approximately 2.87 seconds. The simulation results near the completion of the filling stage are given in figure 4-20 to figure 4-22. Figure 4-21 shows the director orientation distributions in the x-y plane for three different heights in the mould gap width. The temperature distributions are displayed in figure 4-22.

The simulation results when mould temperature equals to 100°C are shown in figure 4-23 to figure 4-26. Figure 4-23 shows the locations of the free surface at various times during the filling operations. The filling time is approximately 4.98 seconds. The simulation results near the completion of the filling stage are given in figure 4-24 to figure 4-26. Figure 4-25 shows the director orientation distributions in the x-y plane for

three different heights in the mould gap width. The temperature distributions are displayed in figure 4-26.

It can be seen that, except in the center, the director orientations align the flowing directions when the mould temperature is 150°C and are irregular when the mold temperature is 100°C.

The shape of the second mould cavity is approximately 7 cm wide, 10 cm long and has a gapwidth of 3 mm.

The simulation results for the second geometry are shown in figure 4-27 to figure 4-30. The mould temperature equals to 200°C. Figure 4-27 shows the locations of the free surface at various times during the filling operations. The filling time is approximately 6.43 seconds. The simulation results near the completion of the filling stage are given in figure 4-28 to figure 4-30. Figure 4-29 shows the director orientation distributions in the x-y plane for three different heights in the mould gap width. The temperature distributions are displayed in figure 4-30.

Except in the central core, Hele-Shaw flows can be treated as simple shear flow. Therefore, the director orientations show phenomenon of aligning when tumbling parameter λ is larger than 1 and tumbling when λ is less than 1. According to table 2 and equation (4-52), λ is a function of temperature, as shown in figure 4-18. Therefore, when the mould temperature is high, the flow near wall is aligning., and the phenomenon of tumbling appears as the mould temperature decreases.

4.4.4 Conclusion

In this section, a numeric simulation approach of injection moulding process of LCPs is presented. This technique can predict the locations of melt front at selected time steps during the injection and the director orientations distributions at various time steps. The LCPs flows are modelled by Leslie-Ericken equations of motion in high viscosity limit. An elliptic pressure equation are derived under Hele-Shaw approximations. The Angular Momentum Equation was solved by a new kind of characteristic integration method. The non-isothermal natures of the flow are modelled by the energy equation shown in section 4.4.2.

Because of the influence of temperature on tumbling parameter λ, the flows of LCPs in skin layers are aligning when the mould temperature is high, and the phenomenon of tumbling appears as the mould temperature decreases.
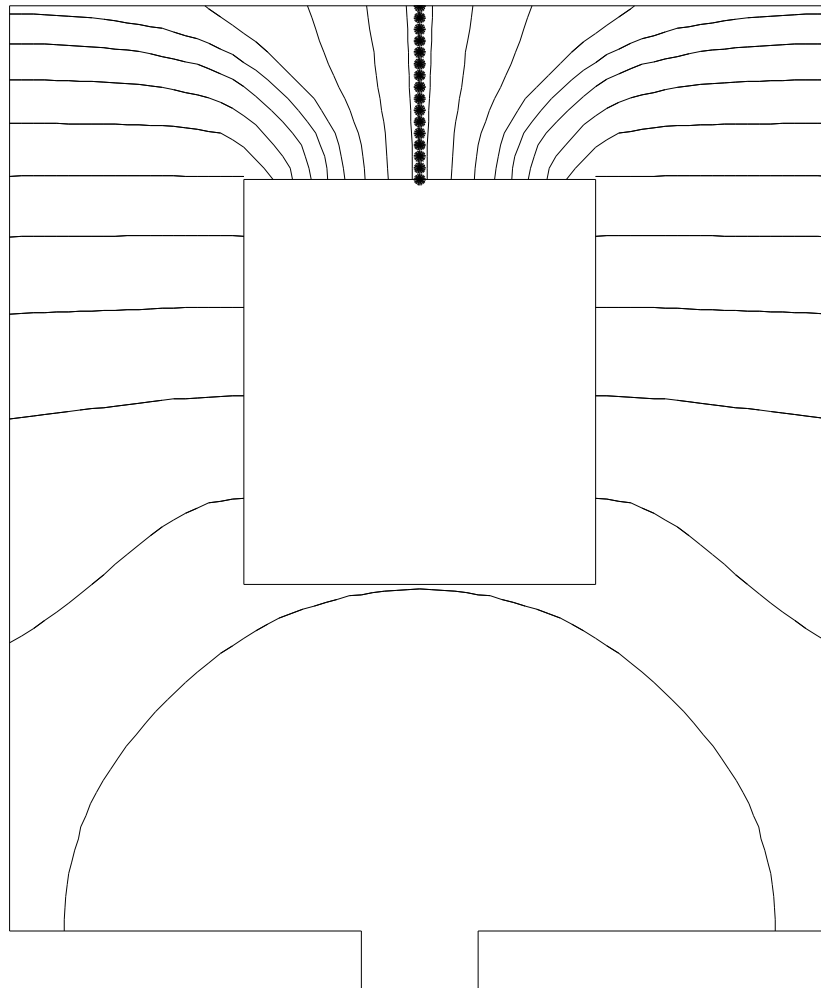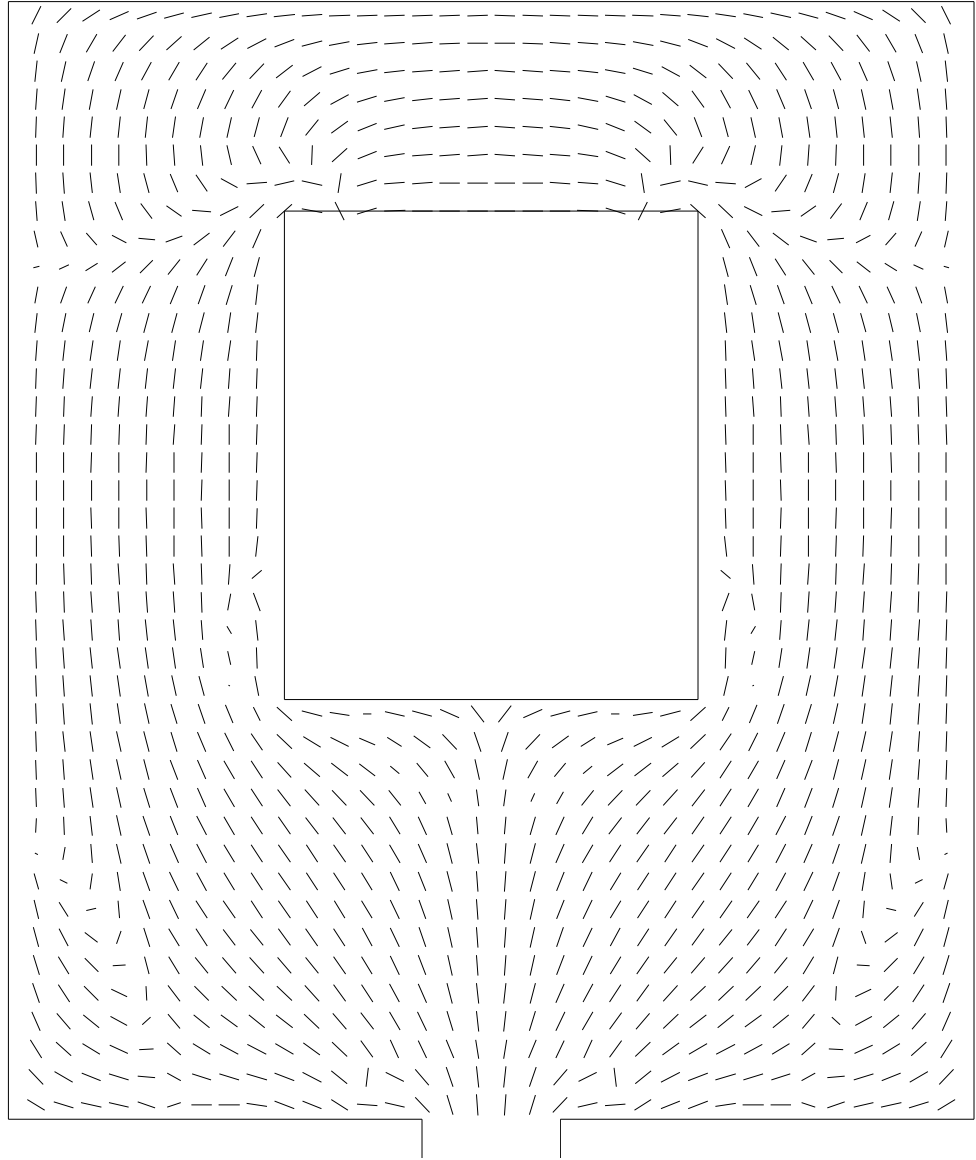

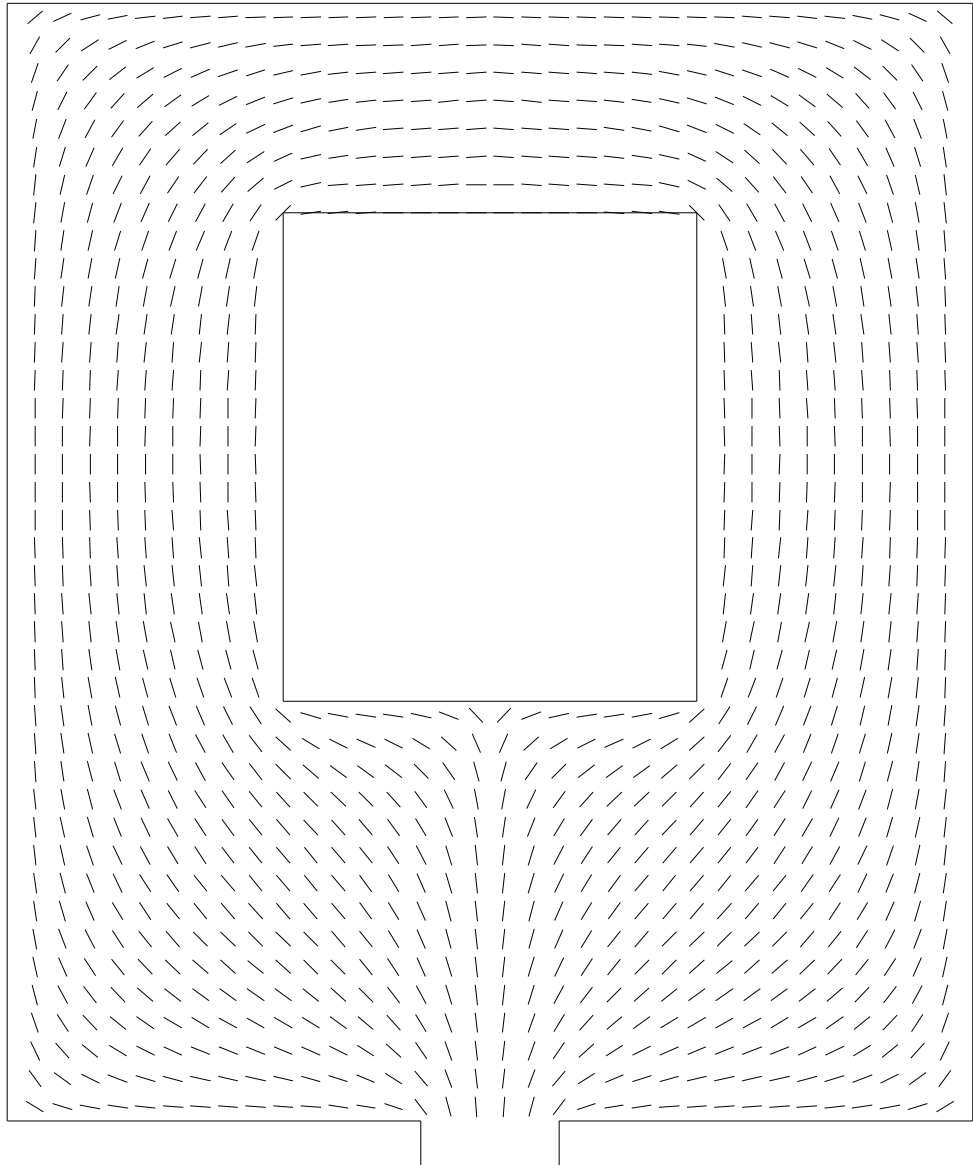Fig 4-19 Development of free surface, time interval= 0.2 second,
mould temperature=150°C

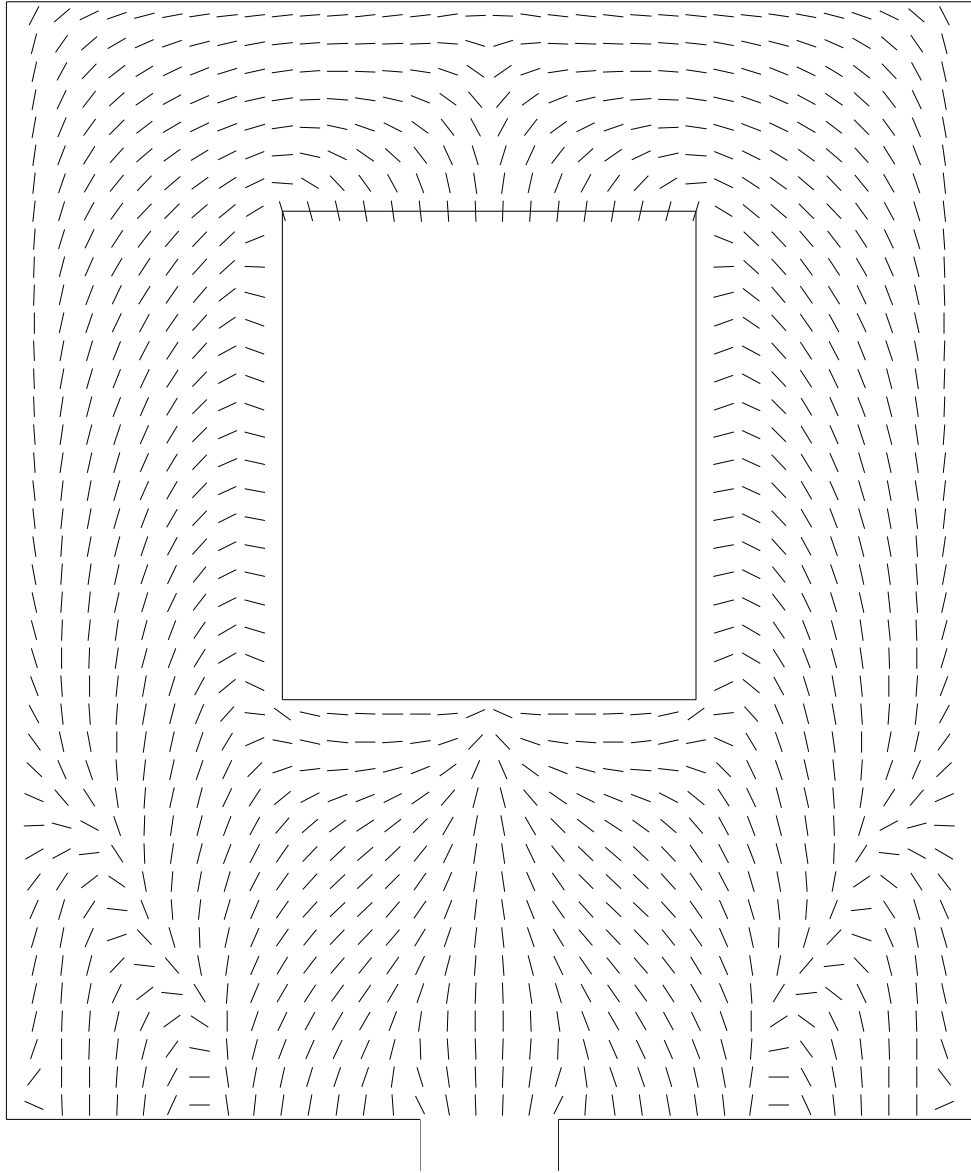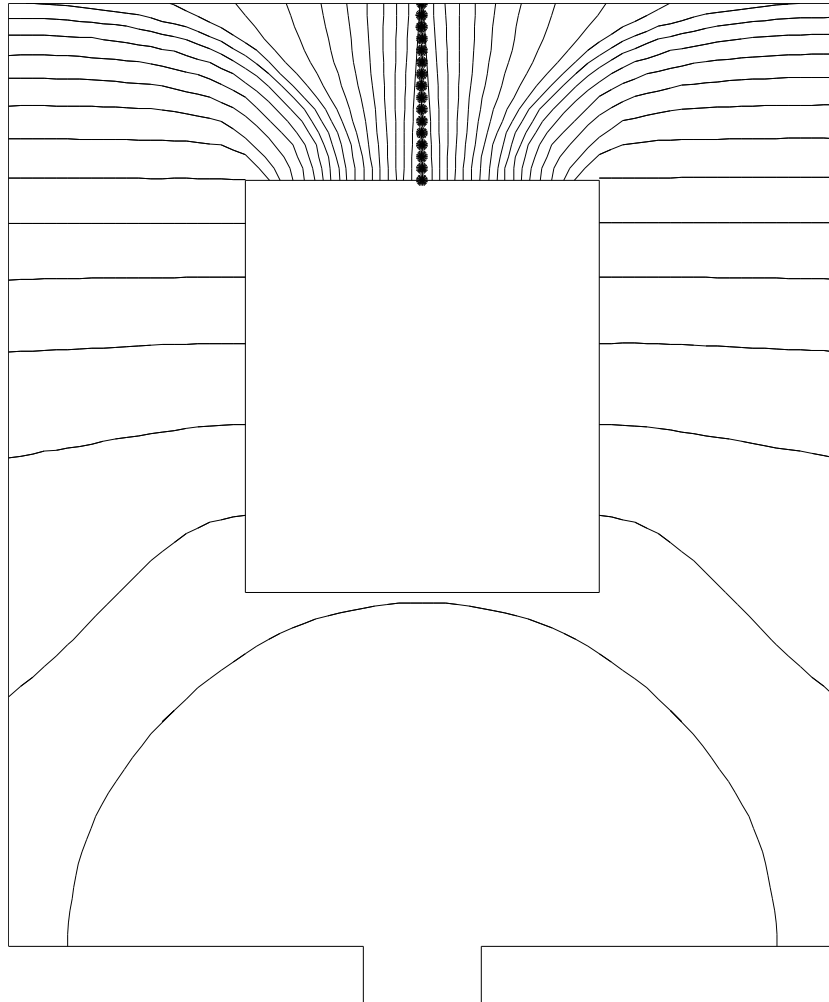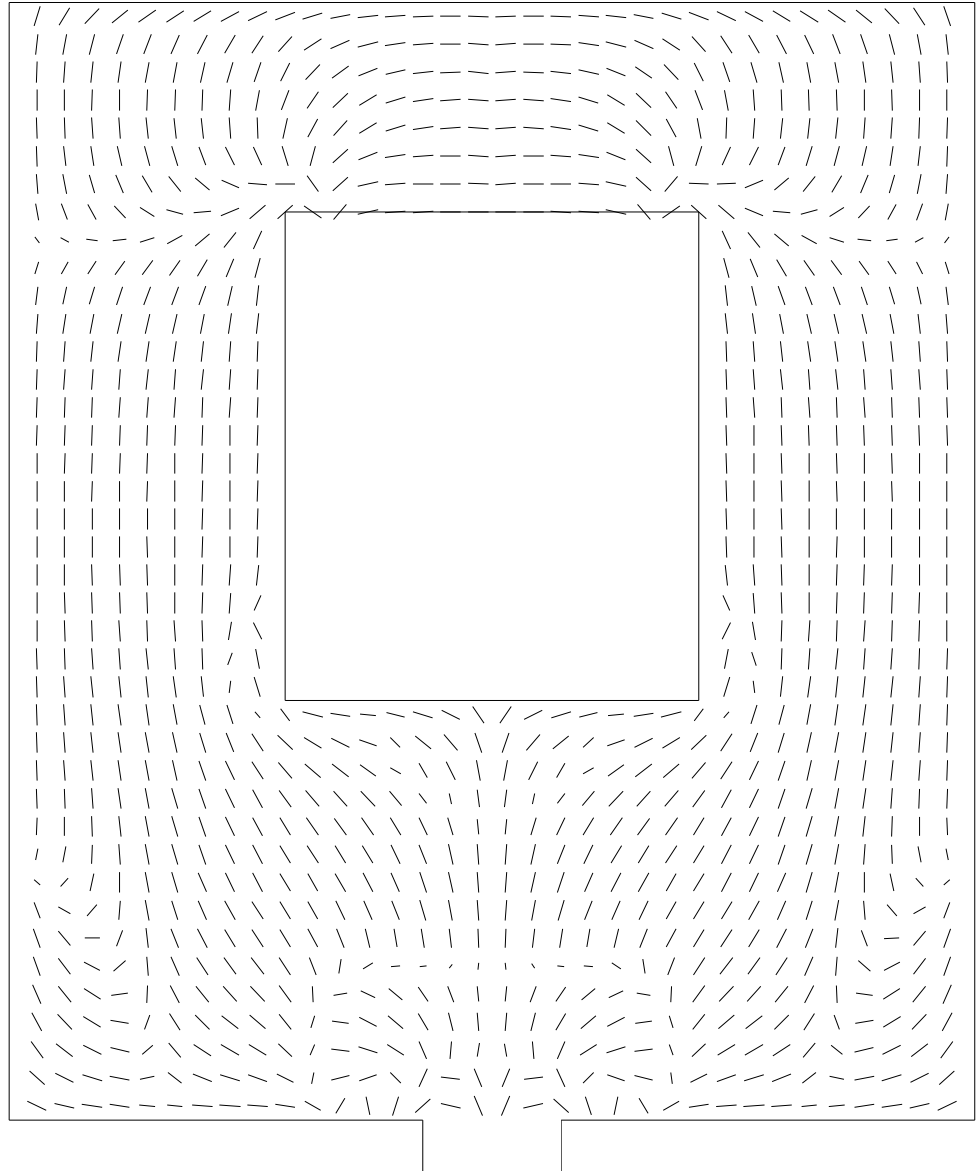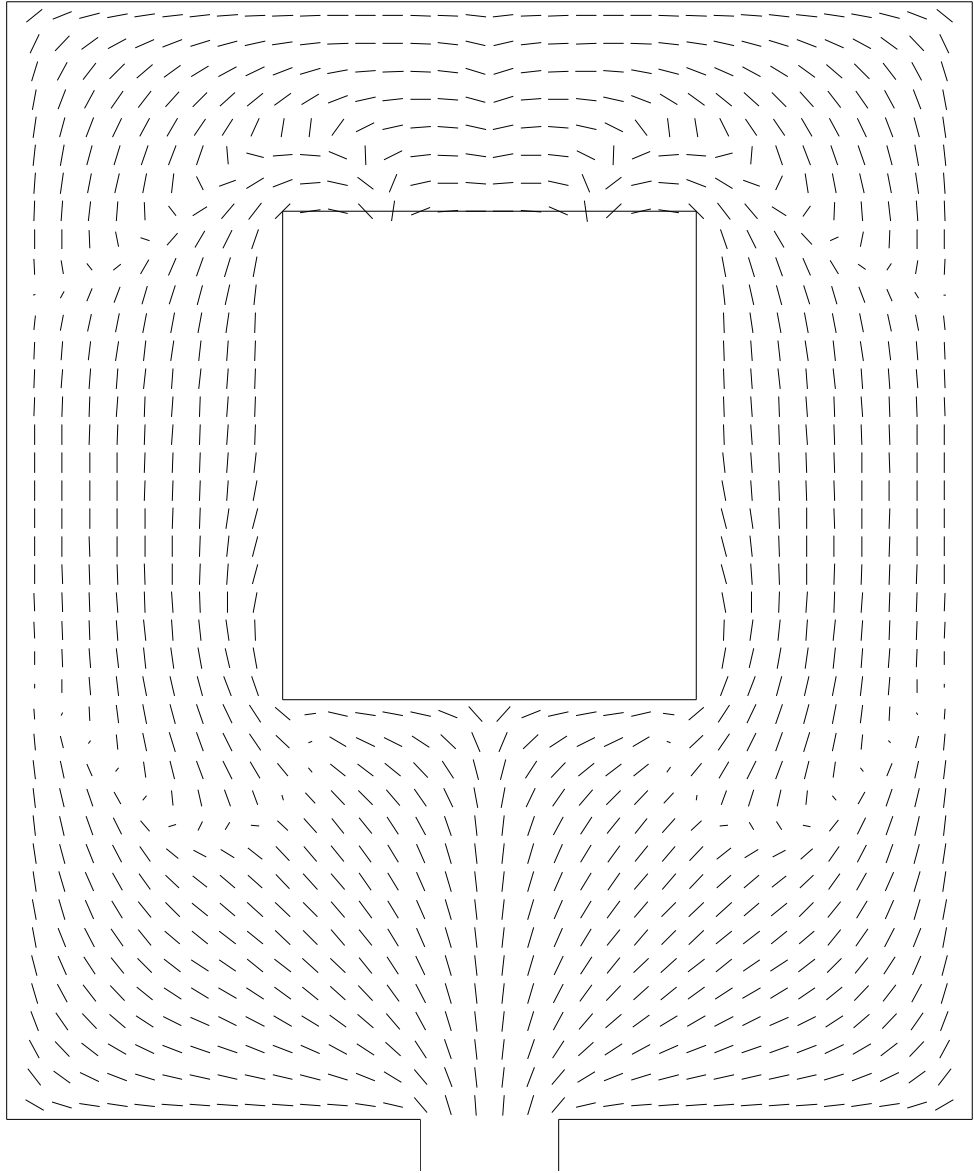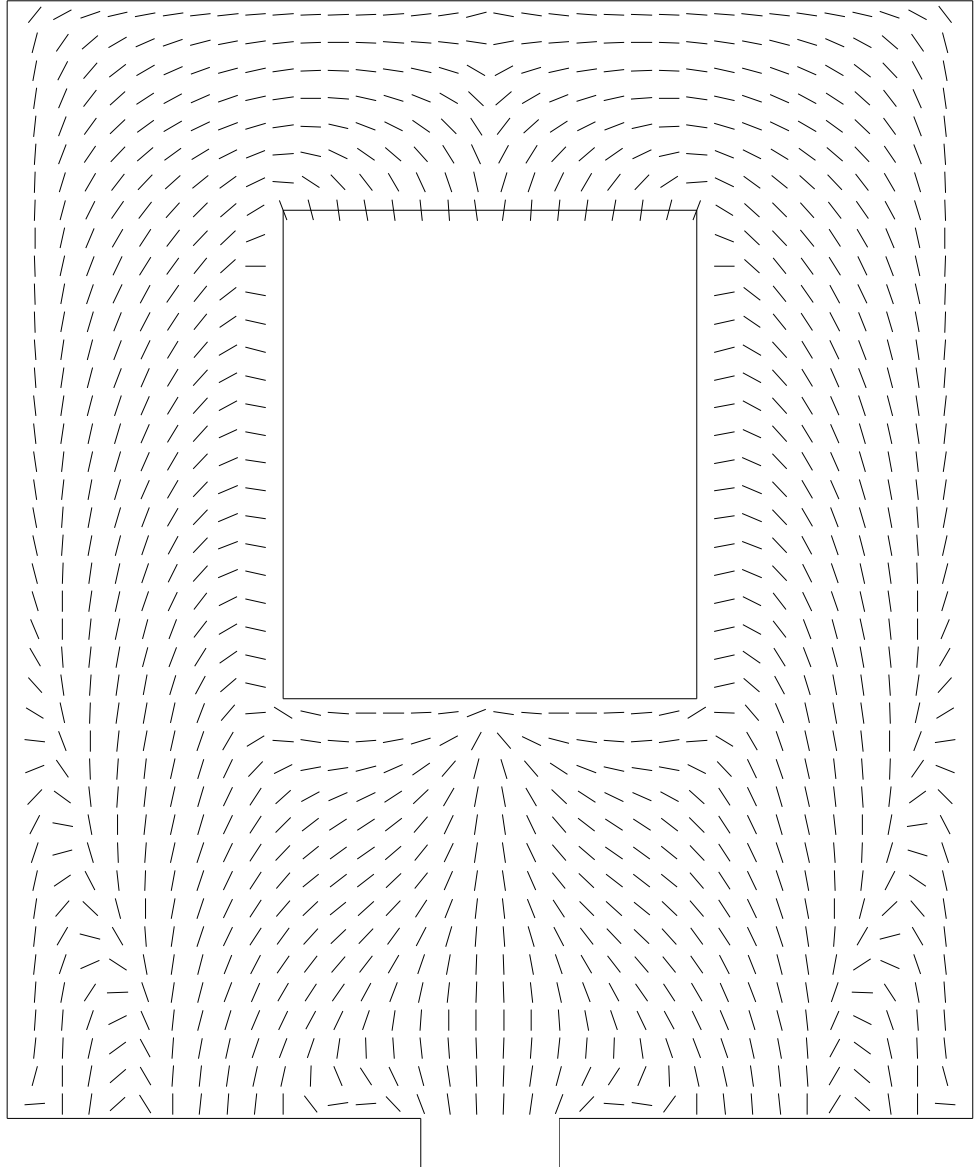Fig 4-20 Pressure distribution (Pa), when mould temperature=150$^{\text{o}}$C

(a) z=0.1 gap size

Fig 4-21 Director orientations at different layers, mould temperature=150$^{\text{o}}$C

(b) z=0.25 gap size

Fig 4-21 continued

(c) z=0.5 gap size (center)

Fig 4-21 continued

(a) z=0.1 gap size

(b) z=0.1 gap size

Fig 4-22 temperature distribution at different layers, mould temperature=150°C

150   300.07

(c) z=0.3 gap size

150   300.02

Fig 4-22 continued   (d) z=0.4 gap size

(e) z=0.5 gap size (center)
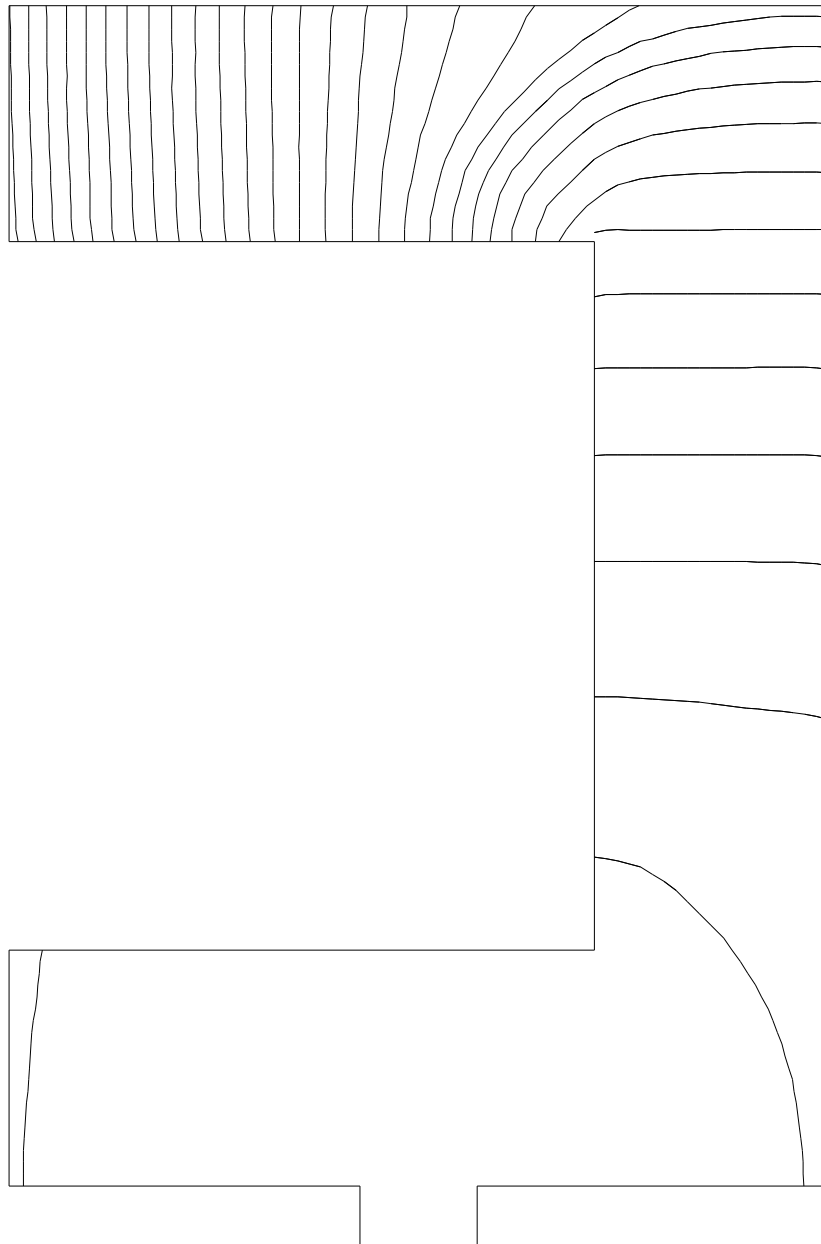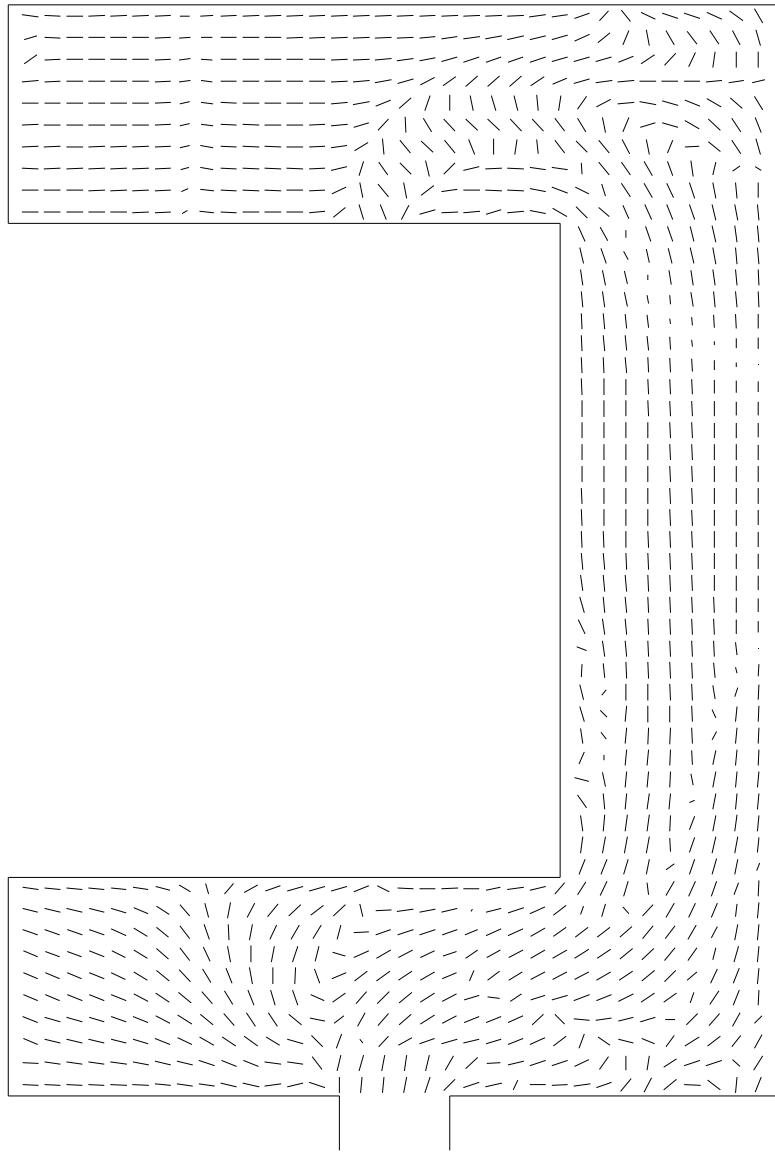
Fig 4-22 continued

Fig 4-23 Development of free surface, time interval= 0.2 sec,
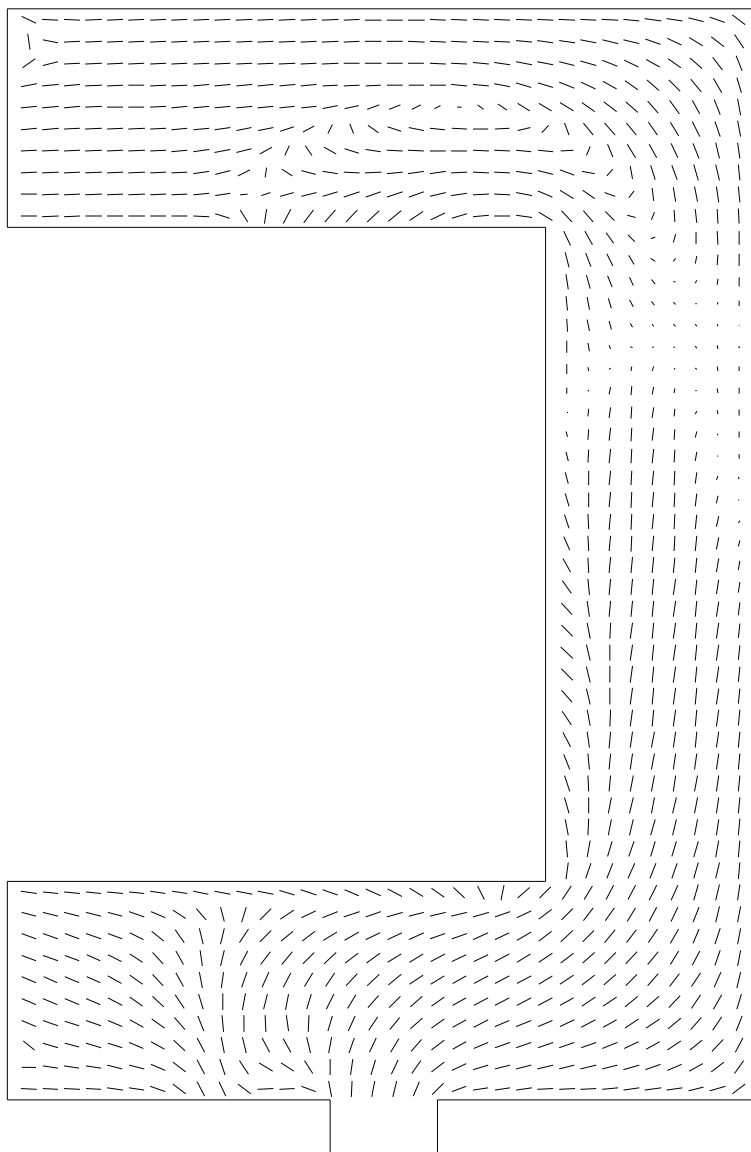mould temperature=100$^{\mathrm{o}}$C

Fig 4-24 Pressure distribution (Pa), when mould temperature=100°C

(a) z=0.1 gap size

Fig 4-25 Director orientations at different layers, mould temperature=100$^{\text{o}}$C

(b) z=0.25 gap size

Fig 4-25 continued

(c) z=0.5 gap size (center)

Fig 4-25 continued

(a) z=0.1 gap size

(b) z=0.2 gap size

Fig 4-26 temperature distribution at different layers, mould temperature=100$^{\mathrm{o}}$C

(c) z=0.3 gap size

Fig 4-26 continued   (d) z=0.4 gap size

(e) z=0.5 gap size

Fig 4-26 continued

Fig 4-27 Development of free surface, time interval= 0.2 sec,
mould temperature=200°C

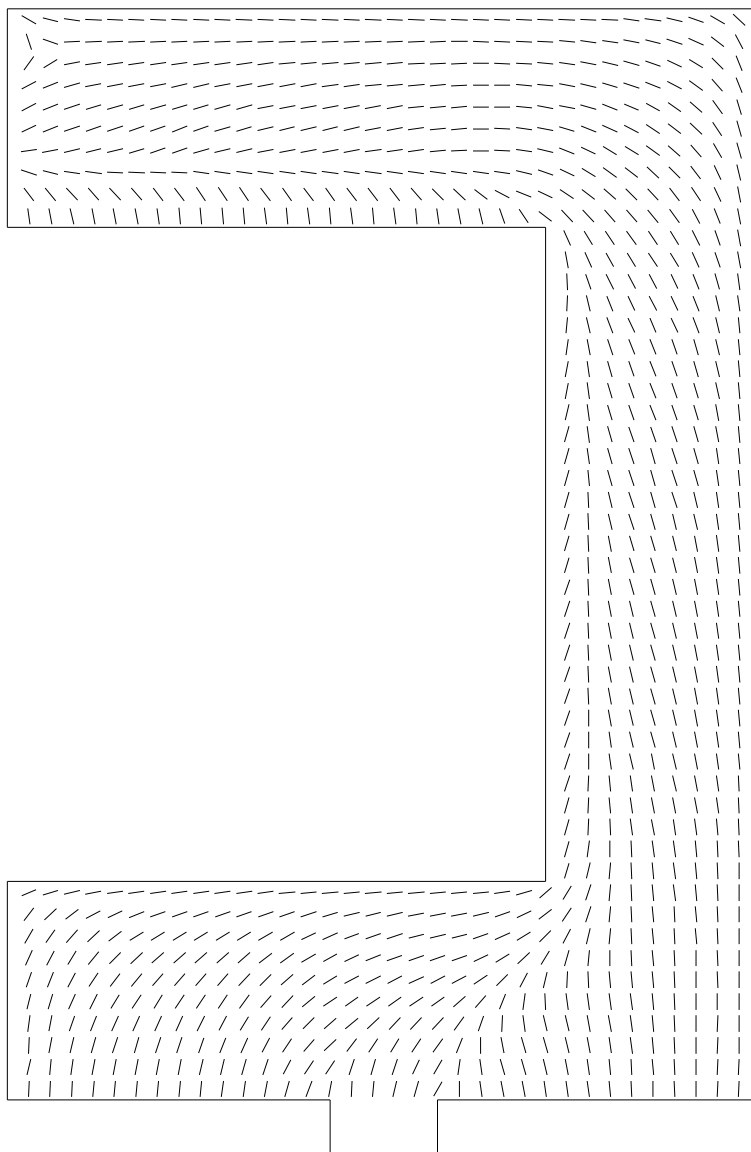Fig 4-28 Pressure distribution (Pa), when mould temperature=200°C

(a) z=0.1 gap size

Fig 4-29 Director orientations at different layers, mould temperature=200°C
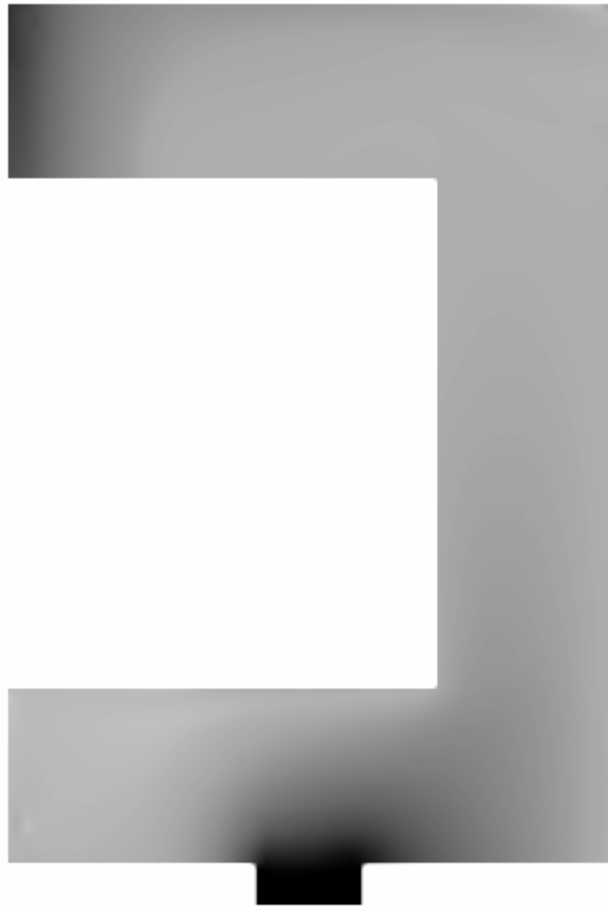
(b) z=0.25 gap size

Fig 4-29 continued

(c) z=0.5 gap size

Fig 4-29 continued

(a) z=0.1 gap size

Fig 4-30 temperature distribution at different layers, mould temperature=200°C

(b) z=0.2 gap size

Fig 4-30 continued

(c) z=0.3 gap size

Fig 4-30 continued

(d) z=0.4 gap size

Fig 4-30 continued

(e) z=0.5 gap size

Fig 4-30 continued

4.5 Simulation of non-isothermal flows into moulds of irregular geometries

Non-isothermal flows of liquid crystalline polymers into two-dimensional thin cavity moulds of irregular shape are simulated in this section. The flows are modelled by the governing equations obtained in section 4.3 and section 4.4. The equations are solved using the finite-difference technique. An improved boundary-fitted mapping technique was developed in this study to solve the difficulty of finite difference treatment of arbitrarily shaped boundaries, which possess no natural coordinate system.

4.5.1 Numerical grid generation

The finite difference treatment of arbitrarily shaped boundaries which possess no natural coordinate system proves more difficult. In general, a body-fitted curvilinear mesh can be generated over any irregular body by essentially mapping the boundaries of the irregular shape from the physical domain to a more regular, prescribe shape in a computational domain. An orthogonal, rectangular mesh can be created on the transformed, simpler domain and then mapped back to provide a curvilinear mesh on the original irregular shape. The governing equations similarly can be transformed and solved on the computational domain, using the well-established finite difference techniques, and the solutions at every node mapped back onto the physical domain.

Usually Poisson type elliptic expressions are used to relate the physical (x,y) coordinates to the computational (ξ,η) coordinates due to their inherent "smoothness" and ability to handle boundary discontinuities. These relations are shown in equation (3-12a) and (3-12b). P and Q are grid control functions that can be used to specify mesh concentration in desired areas.

This scheme has been used successfully in the finite difference solution of the equations for flow about irregularly shaped two-dimensional bodies by many researchers. However, the selection of P and Q is not an easy task, most researchers set them equal to zero. This simplification works well for some situations, but the selection of P and Q is still necessary for flow domains of complicated shapes. To solve this

problem, we developed the so-called "boundary-fitted mapping" technique. As shown in fig 3-4, only the boundaries of flow domain take part in the mapping process. Obviously the mesh concentration control is not necessary and P and Q can be set equal to zero for arbitrarily shaped flow domain. At the grid points on the boundary, the governing equations are transformed and solved on the computational domain, and the solutions at every boundary node were mapped back onto the physical domain. At the grid points inside boundaries, the governing equations are solved on the physical domain directly.

4.5.2 Transformation of the governing equations

In order to compute the finite-difference solutions to the governing equations over the transformed domain, they need to be expressed in terms of the transformed coordinates ξ, η, and z. Based on the coordinate transformation described above, the elliptic pressure equation (4-43) can be expressed as:

$$a_1 \frac{\partial^2 p}{\partial \xi^2} + a_2 \frac{\partial^2 p}{\partial \xi \partial \eta} + a_3 \frac{\partial^2 p}{\partial \eta^2} + a_4 \frac{\partial p}{\partial \xi} + a_5 \frac{\partial p}{\partial \eta} = 0 \tag{4-59}$$

where

$$a_1 = G_1 (\frac{\partial \xi}{\partial x})^2 + (G_2 + G_3) \frac{\partial \xi}{\partial x} \frac{\partial \xi}{\partial y} + G_4 (\frac{\partial \xi}{\partial y})^2 \tag{4-60a}$$

$$a_2 = 2 G_1 \frac{\partial \xi}{\partial x} \frac{\partial \eta}{\partial x} + (G_2 + G_3)(\frac{\partial \xi}{\partial x} \frac{\partial \eta}{\partial y} + \frac{\partial \xi}{\partial y} \frac{\partial \eta}{\partial x}) + 2 G_4 \frac{\partial \xi}{\partial y} \frac{\partial \eta}{\partial y} \tag{4-60b}$$

$$a_3 = G_1 (\frac{\partial \eta}{\partial x})^2 + (G_2 + G_3) \frac{\partial \eta}{\partial x} \frac{\partial \eta}{\partial y} + G_4 (\frac{\partial \eta}{\partial y})^2 \tag{4-60c}$$

$$a_4 = (\frac{\partial G_1}{\partial x} + \frac{\partial G_3}{\partial y}) \frac{\partial \xi}{\partial x} + (\frac{\partial G_2}{\partial x} + \frac{\partial G_4}{\partial y}) \frac{\partial \xi}{\partial y} \tag{4-60d}$$

$$a_5 = (\frac{\partial G_1}{\partial x} + \frac{\partial G_3}{\partial y}) \frac{\partial \eta}{\partial x} + (\frac{\partial G_2}{\partial x} + \frac{\partial G_4}{\partial y}) \frac{\partial \eta}{\partial y} \tag{4-60e}$$

The expressions for ξ and η components of velocity can be obtained as:

$$\overline{v}_\xi = r_1 \frac{\partial p}{\partial \xi} + r_2 \frac{\partial p}{\partial \eta} \tag{4-61a}$$

$$\overline{v}_\eta = r_3 \frac{\partial p}{\partial \xi} + r_4 \frac{\partial p}{\partial \eta} \qquad\qquad\qquad (4\text{-}61b)$$

where

$$r_1 = \frac{\partial \xi}{\partial x}(G_1 \frac{\partial \xi}{\partial x} + G_3 \frac{\partial \xi}{\partial y}) + \frac{\partial \xi}{\partial y}(G_2 \frac{\partial \xi}{\partial x} + G_4 \frac{\partial \xi}{\partial y}) \qquad (4\text{-}62a)$$

$$r_2 = \frac{\partial \eta}{\partial x}(G_1 \frac{\partial \xi}{\partial x} + G_3 \frac{\partial \xi}{\partial y}) + \frac{\partial \eta}{\partial y}(G_2 \frac{\partial \xi}{\partial x} + G_4 \frac{\partial \xi}{\partial y}) \qquad (4\text{-}62b)$$

$$r_3 = \frac{\partial \xi}{\partial x}(G_1 \frac{\partial \eta}{\partial x} + G_3 \frac{\partial \eta}{\partial y}) + \frac{\partial \xi}{\partial y}(G_2 \frac{\partial \eta}{\partial x} + G_4 \frac{\partial \eta}{\partial y}) \qquad (4\text{-}62c)$$

$$r_4 = \frac{\partial \eta}{\partial x}(G_1 \frac{\partial \eta}{\partial x} + G_3 \frac{\partial \eta}{\partial y}) + \frac{\partial \eta}{\partial y}(G_2 \frac{\partial \eta}{\partial x} + G_4 \frac{\partial \eta}{\partial y}) \qquad (4\text{-}62d)$$

Boundary condition for equation (4-59) is:

$$\overline{v}_\eta = 0 \qquad\qquad\qquad\qquad (4\text{-}63)$$

4.5.3 Results and discussion

In this section, the simulation results of the injection moulding of LCPs with constant inlet pressure are presented. The shape of the mould cavity is approximately 7 cm wide, 10 cm long and has a gap width of 3 mm. The melt was considered to enter the cavity at an inlet temperature of 300°C. A constant inlet pressure of 60 atmospheric pressures was assumed during the filling stage.

The simulation results when the mould wall was held at a constant temperature of 250°C were displayed in figure 4-31 to figure 4-33. Figure 4-31 shows the locations of the free surface at various times during the filling operations. The filling time is approximately 9.35 seconds. The simulation results near the completion of the filling stage are given in figure 4-32 and figure 4-33. Figure 4-32 shows the director orientation distributions in the x-y plane for three different heights in the mould gap width. The temperature distributions are displayed in figure 4-33.

The simulation results when mould temperature equals to 200°c are shown in figure

4-34 to figure 4-36. Figure 4-34 shows the locations of the free surface at various times during the filling operations. The filling time is approximately 19.2 seconds. The simulation results near the completion of the filling stage are given in figure 4-35 and figure 4-36. Figure 4-35 shows the director orientation distributions in the x-y plane for three different heights in the mould gap width. The temperature distributions are displayed in figure 4-36.

It can be seen that the director orientations in the skin layers align along the flowing directions when the mould temperature is 250°C and the phenomenon of tumbling appears when the mould temperature decreases to 200°C.

4.5.4 Conclusion

In this section, a numeric simulation approach of injection moulding process of LCPs is presented. This technique can predict the locations of melt front at selected time steps during the injection and the director orientations distributions at various time steps. The LCPs flows are modelled by Ericken-Leslie equations of motion in high viscosity limit. An elliptic pressure equation are derived under Hele-Shaw approximations which was solved by finite difference method. And a new boundary-fitted mapping technique was developed to solve the difficulty of finite difference treatment of arbitrarily shaped boundaries. It can be seen from the simulation results that the new boundary-mapping technique works well.
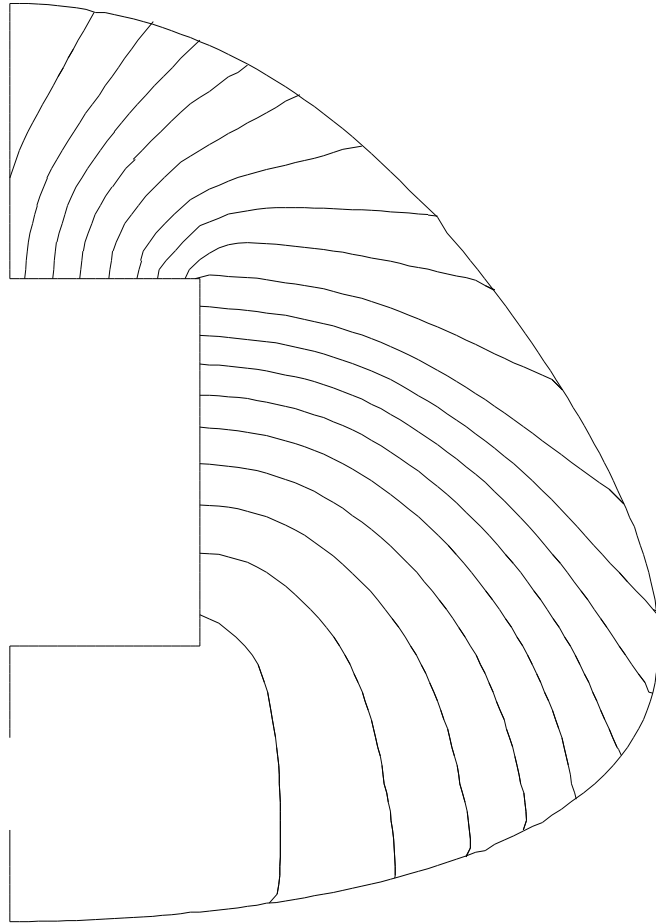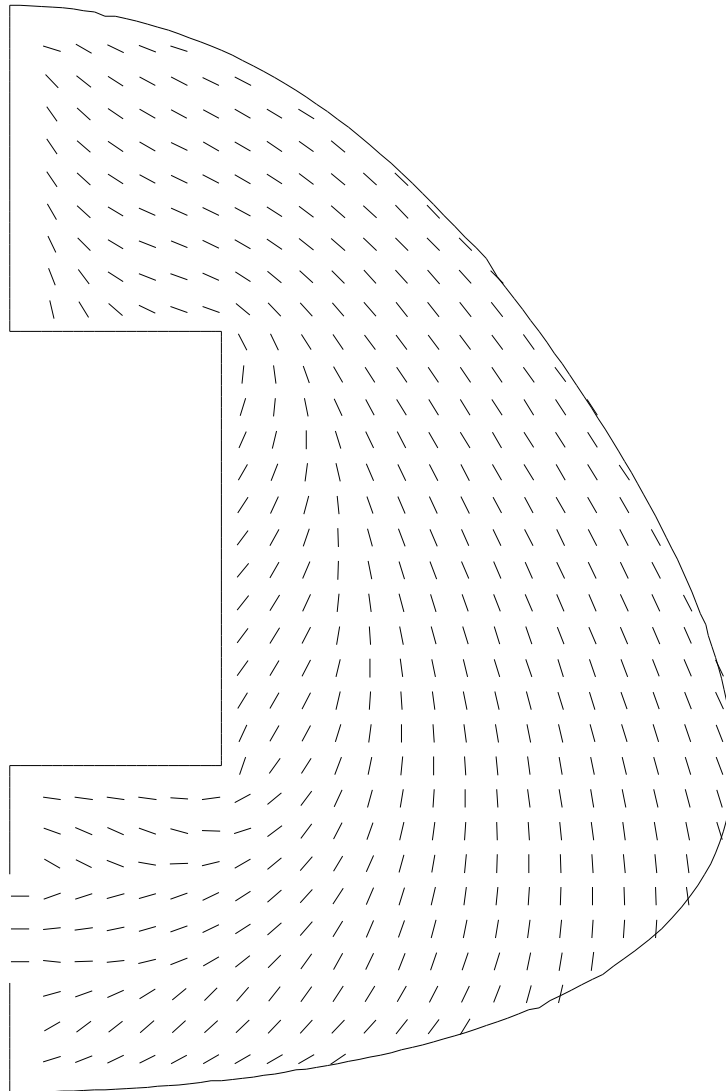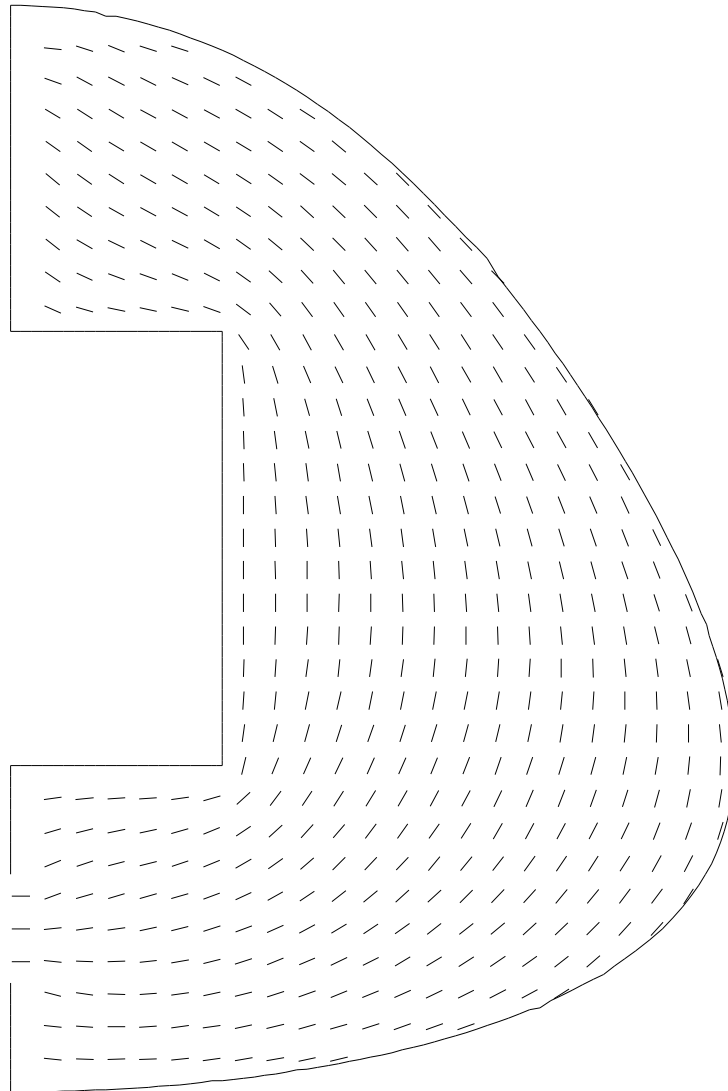
Fig 4-31. free surface locations at varies time, time interval= 0.5 second,
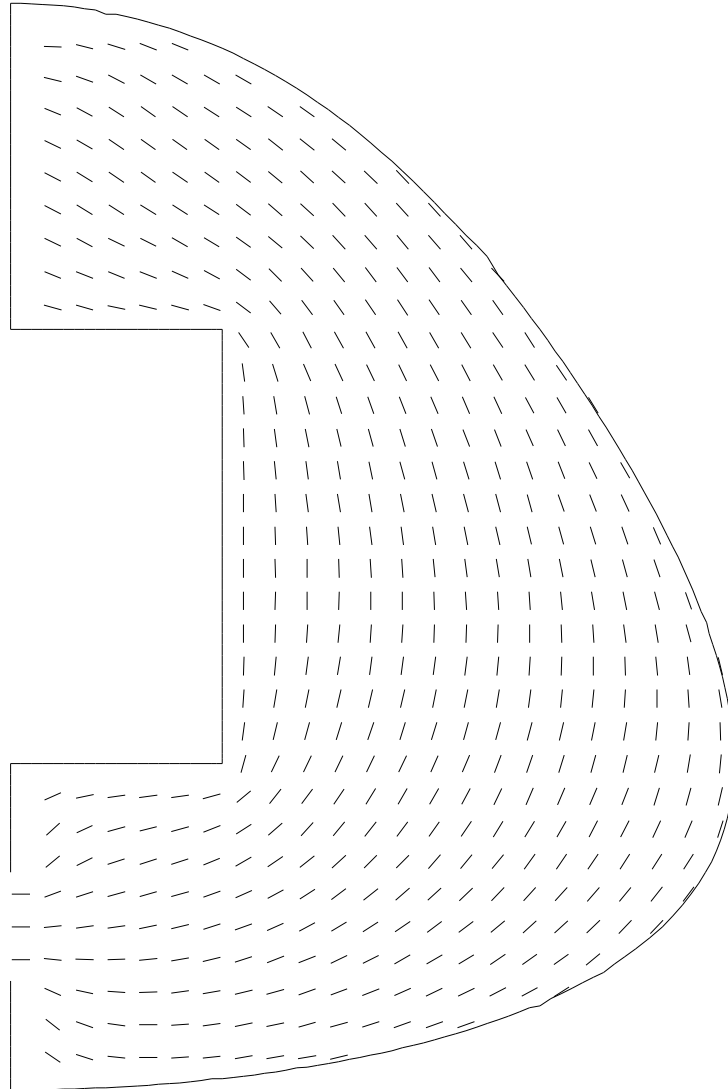mould temperature =250$^{\text{o}}$C

(a) z=0.5 gap size (center)

Fig 4-32. Director orientations at different layers, mould temperature=250$^{\text{o}}$C
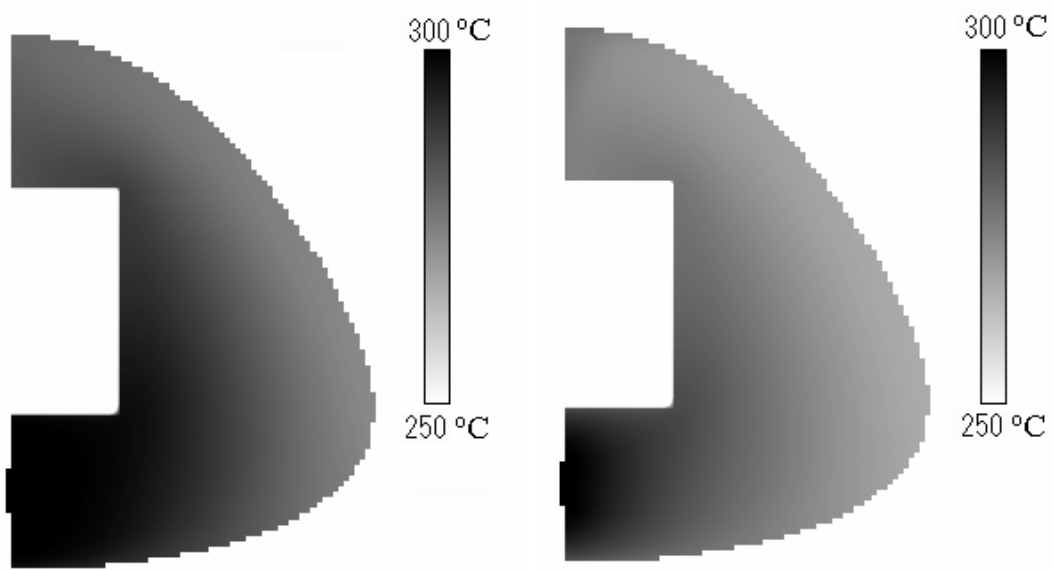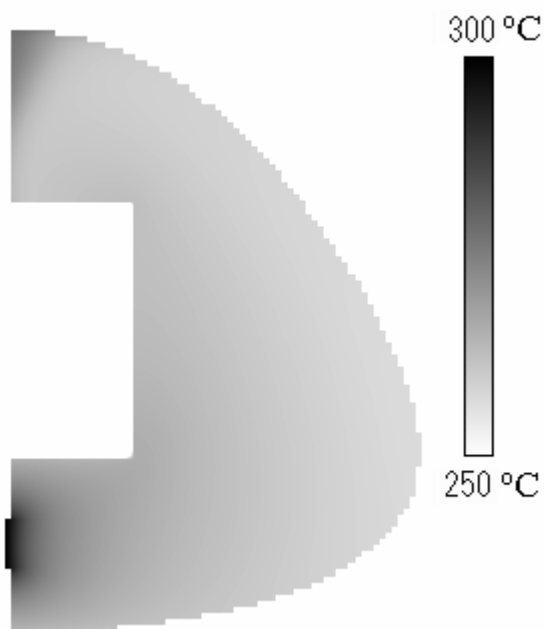
(b) z=0.25 gap size

Fig 4-32 continued

(c) z=0.1 gap size

Fig 4-32 continued

(a) z=0.5 gap size (center)   (b) z=0.25 gap size

(c) z=0.1 gap size

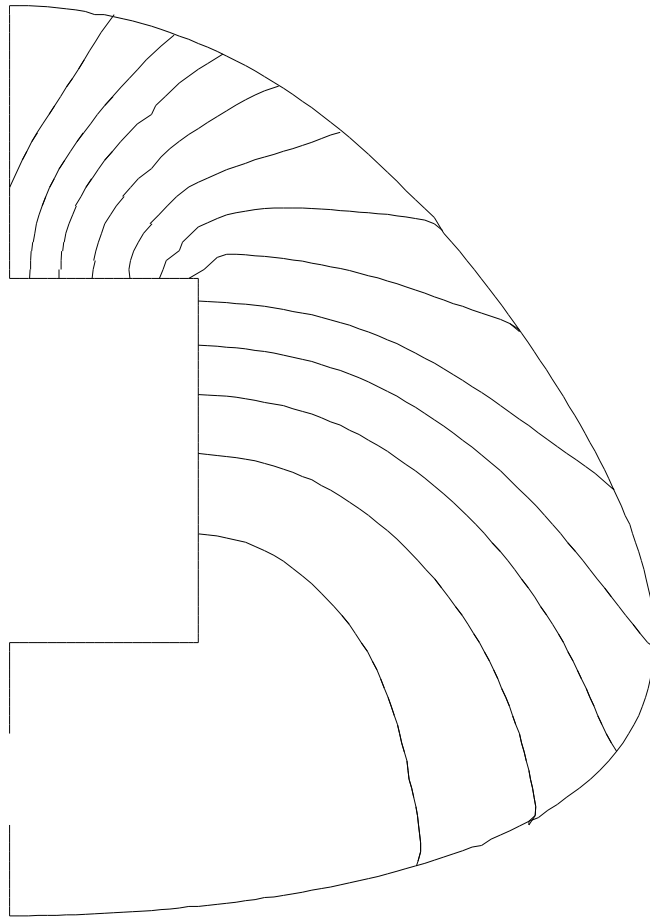Fig 4-33 Temperature distributions at different layers, mould temperature=250°C
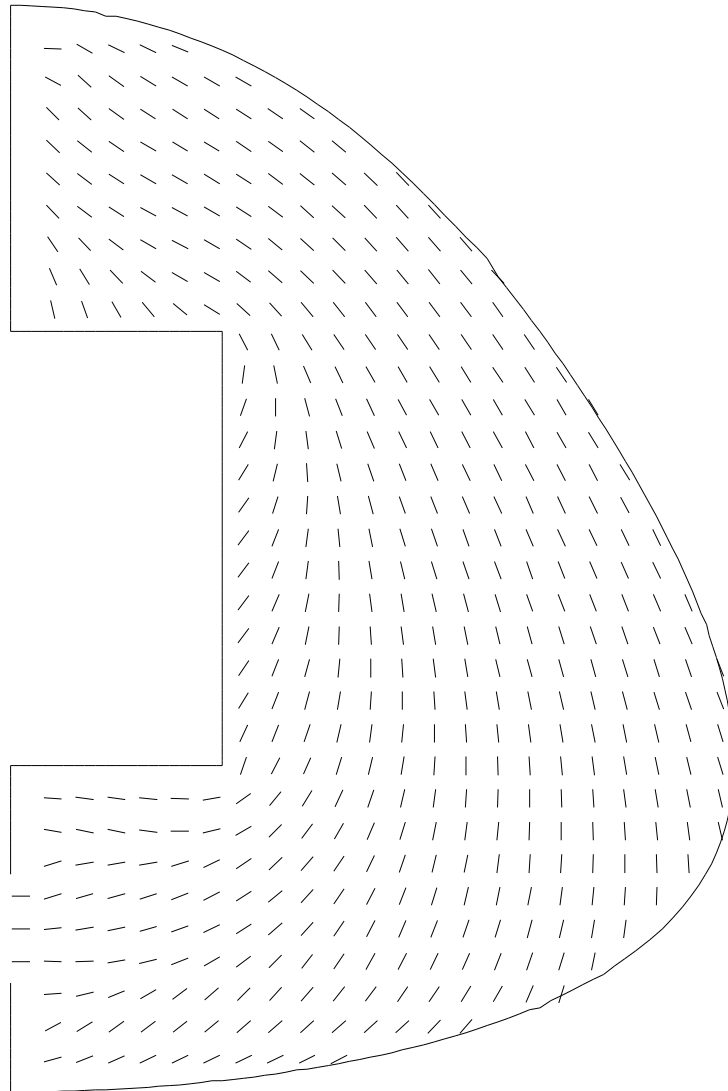
Fig 4-34 The free surface locations at varies time, time interval= 1.5 second,
mould temperature =200$^{\text{o}}$C

(a) z=0.5 gap size (center)

Fig 4-35 Director orientations at different layers, mould temperature=200°C

(b) z=0.25 gap size

Fig 4-35 continued

(c) z=0.1 gap size

Fig 4-35 continued

(a) z=0.5 gap size (center)

(b) z=0.25 gap size

(c) z=0.1 gap size

Fig 4-36 Temperature distributions at different layers, mould temperature=200$^{\text{o}}$C
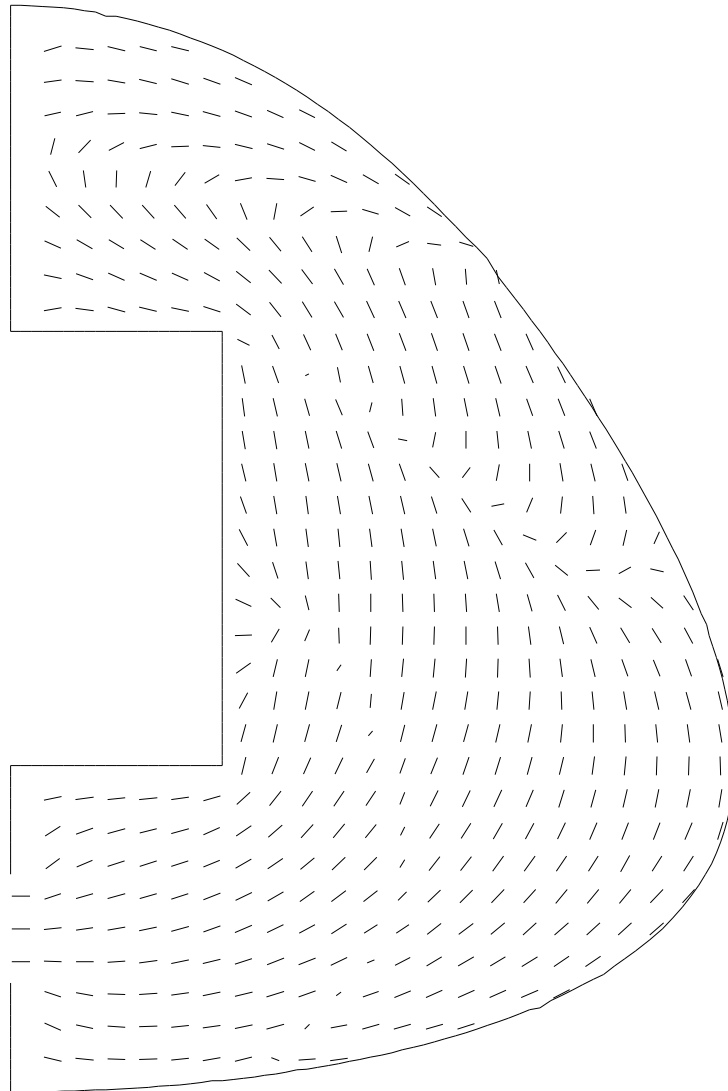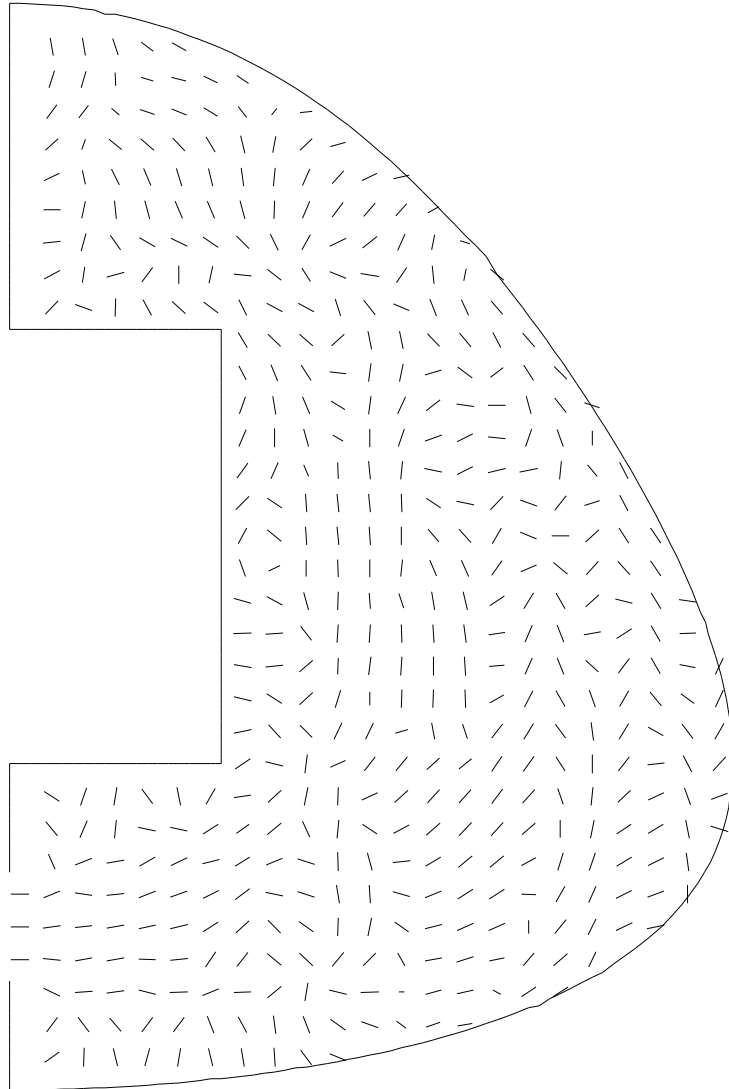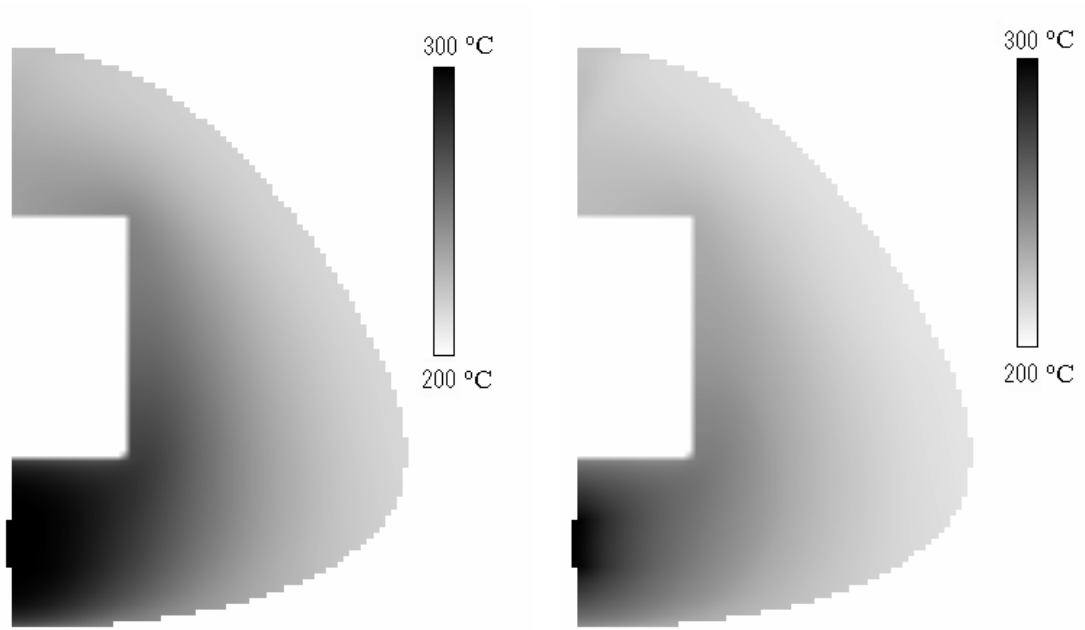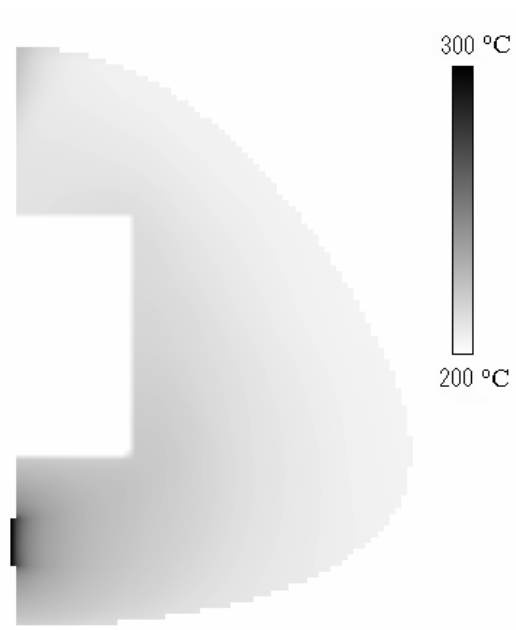
Chapter 5: Conclusion

This dissertation gave a detail presentation of three simulations of LCPs flows into two-dimensional thin cavity moulds. They are:

1. simulation of isothermal flows into mould of regular shape (section 4.3).
2. simulation of non-isothermal flows into mould of regular shape (section 4.4).
3. simulation of non-isothermal flows into mould of irregular shape (section 4.5)

These flows are modelled by Leslie-Ericken equations of motion in high viscosity limit. An elliptic pressure equation are derived under Hele-Shaw approximations in section 4.3. The non-isothermal natures of the flow are modelled by the energy equation shown in section 4.4.2.

In section 4.2, we give an analysis of the steady director of liquid crystal in Hele-Shaw flows. This result may help to explain a widely recognized phenomenon in the moulding process of nematic polymers, which is that the molecular chains in the skin regions are largely aligned along the injection directions while the chain orientations in the central core is more or less random.

The finite difference method was used to solve the governing equations, because of its simplicity and high efficiency. Numerical grid generation technique can remove the problem of boundary shape from finite difference methods. However, the grid control is a difficult task for the numerical grid generation technique in geometries of complicated shape. In section 3.4, we developed the so-called " improved boundary-fitted mapping" technique. This new scheme is much simpler than the original numerical grid generation technique. It frees the computational simulation from restriction to certain boundary shapes and allows general codes to be written in which the boundary shape is specified simply by input. It can help the finite difference method to overcome its difficulty on treating flows in complicated geometries and keep the simplicity and high efficiency of the finite difference method at the same time. It can be seen from the simulation results in section 4.5 that the new boundary-fitted mapping technique work well

Reference

1. Shigeomi CHONO and Tomohiro TSUJI. Computer simulation of flow and defect of nematic liquid crystal, EKISHO(in Japanese), Vol. 3, N0.2, 1999, 107-116

2. Rong-Yeu Chang, Fu-Chia Shiao, and Wen-Lii Yang, Simulation of director orientation of liquid crystalline polymers in 2-D flows, J. Non-Newtonian Fluid Mech., 55 (1994) 1-20

3. Marifi Guler, Symbolic evaluation of the Ericksen-Leslie equations in the computati -on domain, J. Non-Newtonian Fluid Mech., 52 (1994) 309-321

4. J.N. Baleo, M. Vincent, and P. Navard, Finite-element simulation of flow and director orientation of viscous anisotropic fluids in complex 2D geometries, J. Rheol. 36 (4), May 1992, 663-701

5. W.B. Vanderheyden and G. Ryskin, Computer simulation of flow and molecular orientation in liquid crystal polymers, J. Non-Newtonian Fluid Mech., 23 (1987) 383- 414

6. C. Lekarou, Mathematical Modeling and Computer Simulations of the Flow, Nematic Phase Orientation, and Heat Transfer in Thermotropic Liquid Crystalline Polymers, Polym. Eng. Sci., March 1997, Vol. 37, No.3, 529-540

7. S. Subbiah, D. L. Trafford and S. I. Guceri, Non-isothermal flow of polymers into two-dimensional, thin cavity molds: a numerical gid generation approach, Int. J. Heat Mass Transfer Vol. 32, No. 3, 415-434 (1989)

8. M. Cengiz Altan, S. Subbiah, Selcuk I. Gucerl and R. Byron Pipes, Numerical Prediction of three-dimensional fiber orientation in Hele-Shaw flows, Polym. Eng. Sci., July 1990, Vol 30, No. 14, 848-859

9. Alejandro D. Rey and Morton M. Denn, Analysis of converging and diverging flow of nematic liquid crystal polymers, Mol. Cryst. Liq. Cryst., 1987, Vol. 153, pp. 301-310

10. C.L. Choy, W.P. Leung and K.W. Kwok, Thermal diffusivity of an injection-moulded liquid crystalline polymer by flash radiometry, Polym. Commun. 1991, Vol. 32, No. 9, pp 285-288

11. Ronald G. Larson, The structure and Rheology of Complex Fluids, Oxford University Press, 1999

12. I. Heynderickx, W. Potze, E.J.W. Ter Maten, Influence of a temperature gradient on the simple shear flow of a nematic liquid crystal, J. Non-Newtonian Fluid Mech., 55 (1994) 137-161.

13. Virtual textbook at http://plc.case.edu/tutorial/enhanced/files/textbook.htm by Case Liquid Crystal and Complex Fluids Group Department of Physics, Case Western Reserve University, Cleveland, Ohio

14. Suresh G. Advani, Flow and rheology on polymer composites manufacturing, 1994, ELSEVIER SCIENCE B.V.

15. M.J.Crochet, A.R.Davies, and K.Walters, Numerical simulation of Non-Newtonian flow, 1984, ELSEVIER SCIENCE B.V

16. XuefengWang, Jonathan Engel and Chang Liu, Liquid crystal polymer (LCP) for MEMS: processes and applications, J. Micromech. Microeng. **13** (2003) 628–633

17. Jianjun Tao and James J. Feng, Effects of elastic anisotropy on the flow and orientation of sheared nematic liquid crystals, J. Rheol. 47~4!, 1051-1070 July/August ~2003

18. Joe F. Thompson, Z. U. A. Warsi, and C. Wayne Mastin, Numerical Grid Generation: Foundations and Applications, 1985, Elsevier Science Publishing Co., Inc.

19. Yu-Chuan Su, Jatan Shah, and Liwei Lin, Implementation and analysis of polymeric microstructure replication by micro injection molding, J. Micromech. Microeng. 14 (2004) 415–422

20. Hieber C A and Shen S F, A finite-element/finite-different simulation of the injection-molding filling process, *J. Non-Newtonian Fluid Mech.* 1982, **71**–32

21. Liquid crystal, From Wikipedia, the free encyclopedia at:
http://en.wikipedia.org/wiki/Liquid_crystal#Liquid_crystal_phases

22. Tomas Carlsson and Christian Hogfors, Theoretical analysis of the stability of shear flow of nematic liquid crystals with a positive Leslie viscosity α_3, J. of Non-Newtonian Fluid Mechanics, Volume 119, Issues 1-3, 1 May 2004, Pages 25-37

23. A. M. Sonnet, P. L. Maffettone and E. G. Virga, Continuum theory for nematic liquid crystals with tensorial order, J. of Non-Newtonian Fluid Mechanics, Volume 119, Issues 1-3, 1 May 2004, Pages 51-59

24. Daniel Lhuillier and Alejandro D. Rey, Nematic liquid crystals and ordered micropolar fluids, J. of Non-Newtonian Fluid Mechanics, Volume 120, Issues 1-3, 1 July 2004, Pages 169-174

25. Shigeomi Chono, Tomohiro Tsuji and Morton M. Denn, Spatial development of director orientation of tumbling nematic liquid crystals in pressure-driven channel flow, J. of Non-Newtonian Fluid Mechanics, Volume 79, Issues 2-3, 1 November 1998, Pages 515-527